FIBER OPTIC FABRY-PÉROT INTERFEROMETRIC SENSOR FOR TEMPERATURE AND STRAIN MEASUREMENT

By

Hasanur R. Chowdhury

A DISSERTATION

Submitted to
Michigan State University
in partial fulfillment of the requirements
for the degree of

Electrical Engineering—Doctor of Philosophy

2023

ABSTRACT

High accuracy temperature and strain measurements are prerequisites for many modern industries to ensure safety, improve efficiency, and reduce greenhouse gas emissions. Traditional thermocouples or electronic devices often encounter challenges in temperature and strain measurement due to cross-sensitivity to surrounding perturbations, sensor's drift at elevated temperature, or susceptibility to electromagnetic interference (EMI). To overcome these, fiber-optic sensors have gained popularity due to their unique advantages, including small size, multiplexing capacity, and immunity to EMI. In this work, we reported a novel approach to measure temperature using fiber optic Fabry-Pérot (FP) interferometer, which eliminates cross-strain sensitivity, shows linearity at high temperature, and provides high accuracy for a broad range. In addition, we developed another sensor for simultaneous measurement of temperature and strain using cascaded fiber Bragg grating (FBG)-silicon FP interferometer configuration.

Our proposed temperature measurement method is based on an air-filled FP cavity, whose spectral notches shift due to a precise pressure variation in the cavity. For fabrication, a fused-silica tube is spliced with a single mode fiber at one end and a side-hole fiber at the other to form the FP cavity. The pressure in the cavity can be changed by passing air through the side-hole fiber causing the spectral shift, which is the measurand of temperature. We have developed two novel approaches based on this setup. The first approach employs two pressure values, their corresponding interferometric valley wavelengths, and the gas material's constant (α) to obtain temperature. A computer-controlled pressure calibration and sensor interrogation system has been developed with miniaturized instruments for this sensor operation. Experimental results show that the sensor has a high wavelength resolution (<0.2 pm) for minimal pressure fluctuation (2.5 × 10⁻³ psi) up to a broad temperature range (over 800 °C). We analyzed the effect of wavelength noise and pressure fluctuation on temperature resolution, which reveals that our developed system can obtain a high resolution (±0.32 °C) temperature measurement. The use of gas as the sensing material and the measurement mechanism also implies long-term stability and eliminates the cross-sensitivity to strain.

In the second approach, we used a pair of FP cavities filled with gas of identical but variable pressure. One of the FPs (reference FP) is placed in the cold zone with a known temperature. The temperature of the measuring FP can be deduced by the spectral fringe shift vs. pressure of the two FPs. This method does not require measurement of the pressure or the knowledge of the optical properties of the gas. Hence it facilitates to make the instrumentation simpler and cost-effective and data acquisition faster. We have verified this method experimentally up to $800 \,^{\circ}$ C. The sensor shows good linearity in the range. Long-term test conducted at $800 \,^{\circ}$ C exhibited the stability of the sensor with fluctuations of $\leq 0.3\%$ over a duration exceeding 100 hours.

In addition to these air-filled FP interferometers, we have presented another novel sensor based on cascaded fiber Bragg grating (FBG)- silicon FP interferometer (FPI) for simultaneous measurement of temperature and strain. The sensor is composed of a 5 mm grating on a single mode fiber and a 100 μ m silicon tip attached to the end of it by UV curable glue. The silicon tip is unbonded, and free from strain whereas the FBG is attached to the host structure. The sensor is tested from room temperature to 100 °C with varying strain up to ~150 $\mu\epsilon$. The silicon FPI provides high temperature sensitivity of 89 pm/°C unaffected by strain. On the contrary, the FBG is affected by both thermal and mechanical strain; the sensitivity of these are experimentally obtained as 32 pm/°C and 1.09 pm/ $\mu\epsilon$, respectively. With a high-speed spectrometer, the temperature and strain resolution of the FPI and FBG are found $\pm 1.9 \times 10^{-3}$ °C and ± 0.042 $\mu\epsilon$, respectively. Due to the small size, enhanced sensitivity and high resolution, this cascaded FBG-FPI sensor can be used in practical applications where accurate measurement of temperature and strain are required.

ACKNOWLEDGEMENTS

I would like to express my profound appreciation to my supervisor, Dr. Ming Han, for his unwavering guidance, support, trust, and encouragement during my academic journey and research at Michigan State University (MSU). My heartfelt gratitude extends to the other members of my committee, Dr. Tim Hogan, Dr. Wen Li, and Dr. Zhen Qiu, for their invaluable assistance throughout my research.

I extend my thanks to my colleagues, both past and present. I am particularly grateful to Dr. Guigen Liu, Dr. Qiwen Sheng, Dr. Yupeng Zhu, Dr. Farzia Karim, Dr. Yufei Chu, Xiaoli Wang, Mohammed Alshammari, and Musaddeque Syed for their collaboration. Working alongside them has been a tremendous learning experience, and their contributions have greatly enriched my research across various projects.

I also acknowledge the essential support provided by Brian Wright, our dedicated ECE technician, who assisted me in countless experimental setups. Furthermore, my appreciation extends to the ECE staff, especially Lisa Clark, Roxanne Peacock, Meagan Kroll, Laurene Rashid, and others who have facilitated our academic and research endeavors.

I am deeply grateful to my friends and colleagues at Michigan State University, with special mention to Dr. Al Ahsan Talukder, Dr. Tamanna TK Munia, Dr. Sami Shokrana, and Dr. Asif Iqbal, for their company and support in our daily lives, making me feel at home despite living thousands of miles away from my home country.

My family holds a special place in my heart, with my parents consistently encouraging my pursuit of higher education. Their unwavering support and inspiration have made my journey possible this far.

Lastly, my deepest gratitude goes to my wife, Zaheda Akthar, for her unwavering support, exceptional patience, constant encouragement, and dedication. Her profound love and belief in me and her role as a wonderful mother to our son, Hamza Chowdhury, have been a source of my strength and inspiration throughout this endeavor.

TABLE OF CONTENTS

LIST OF TABLES	vi
LIST OF FIGURES	vii
CHAPTER 1 INTRODUCTION	1 1 4 8
CHAPTER 2 TEMPERATURE MEASUREMENT USING AIR-FILLED FABRY-	
PÉROT CAVITY WITH VARIABLE PRESSURE	9
2.1 Introduction	9 10 12 14 15 17
	24
	25
3.1 Introduction	27 27 28 30 33 36 38
4.1 Introduction	39 39 41 43 46 52
5.1 Temperature measurement using air-filled FP cavity	54 54 58
BIBLIOGRAPHY	60

LIST OF TABLES

Table 2.1	Optimized splicing parameter for fabrication	11
Table 2.2	Comparison of temperature measurement by our sensor and a reference thermocouple	24
Table 4.1	Comparison of silica and silicon materials	45
Table 5.1	High melting point materials for reference	58

LIST OF FIGURES

Figure 1.1	Schematic of a typical FP interferometer sensor	3
Figure 1.2	Schematic of a typical fiber optic sensor interrogation setup	۷
Figure 2.1	(a) Schematic of the sensor; (b) and (c) cross-section of silica tube and sidehole fiber, respectively.	11
Figure 2.2	Fabrication process of the Fabry-Pérot fiber-optic interferometer sensor	12
Figure 2.3	(a) Microscopic longitudinal view of the fabricated sensor; (b) reflection spectrum of the sensor at ambient temperature and pressure	13
Figure 2.4	Schematics of the fiber-optic temperature sensor system	16
Figure 2.5	Flowchart of the temperature measurement system algorithm	17
Figure 2.6	(a) Reflection spectrum of an FP sensor with a threshold line to define valleys,(b) curve fitting for wavelength detection	18
Figure 2.7	Reflection spectra for two different pressure levels at (a) room temperature and (b) $800^{\circ}\mathrm{C}$ temperature	19
Figure 2.8	Spectral shift with pressure at different temperatures	20
Figure 2.9	Linear relationship between temperature T and S	20
Figure 2.10	Sensor wavelength resolution at room temperature for (a) 0 psi_g and (b) 100 psi_g pressure	21
Figure 2.11	Sensor wavelength resolution for two different pressure levels at each measurement.	22
Figure 2.12	Pressure fluctuation δP_2 at each measurement	22
Figure 2.13	Temperature resolution δT obtained for various temperature T	23
Figure 3.1	Schematics of (a) the sensor system with dual FPs, and (b) spectral shifts with pressure for both FPs	29
Figure 3.2	Schematic of the sensor	31
Figure 3.3	Cross sectional view of (a) silica-tube and (b) side-hole fiber, respectively, used in FP sensor fabrication, (c) and (d) microscopic view of the fabricated sensors.	31
Figure 3.4	Reflection spectra of the sensors at room temperature and room pressure	32

Figure 3.5	Schematic of experimental set up for testing the dual FP sensor system	32
Figure 3.6	Flowchart of the program developed for real-time measurement	33
Figure 3.7	(a,b) Reflection spectra of the reference FP at room temperature (a) and measuring FP at 800 °C (b) at two different pressure levels, (c) measured temperature vs set temperature in the furnace	34
Figure 3.8	(a) Standard deviation (resolution) of fringe valley wavelength determination at different temperatures of the reference FP and the measuring FP, (b) temperature resolution from room temperature to $800^{\circ}\mathrm{C.}$	36
Figure 3.9	Long-term stability test: measured temperature at different times when the furnace was set to 800 $^{\circ}\mathrm{C}$ (1073 K) for 100 hours	37
Figure 4.1	Sensor schematic diagram (dimensions are not proportionately scaled)	42
Figure 4.2	Fabrication method of FBG by Excimer laser	42
Figure 4.3	Strain distribution profile over FBG length	42
Figure 4.4	Reflection spectrum of the FBG-FPI sensor at room temperature	43
Figure 4.5	Experimental setup for temperature test	46
Figure 4.6	Reflection spectra at various temperature. The two red arrows indicate the shift of the left most and right most valley. Grey shaded valleys are affected by FBG shift, hence are filtered out for average wavelength measurement	47
Figure 4.7	(a) Wavelength shift of the FP valleys with temperature, (b) wavelength resolution measured over 10s	48
Figure 4.8	Experimental (cantilever) setup for strain measurement	49
Figure 4.9	(a) Wavelength shift of the FBG peak with strain, (b) wavelength resolution of the FBG peak at initial condition	50
Figure 4.10	Comparison of FBG peak wavelength shift with temperature for unbonded and bonded sensor	51
Figure 4.11	(a) FPI and (b) FBG wavelength shift with varying temperature and strain (insets show the zoomed-in view of a specific temperature data)	52
Figure 5.1	Modified configuration with side-hole fiber as lead-in fiber	56
Figure 5.2	Modified setup with an additional air drier to maintain constant humidity	57

CHAPTER 1

INTRODUCTION

1.1 Research Background

Temperature and strain are two key parameters that need to be monitored and controlled precisely in a wide range of applications, including industrial, chemical, structural, biomedical, and environmental aspects. Most traditional tools to measure temperature and strain are based on electronic devices or thermocouples. However, in the case of rigorous environments such as high-temperature, high-corrosivity, or high-pressure environments, these electronic devices and thermocouples meet significant challenges for accurate measurement. Any alternative mechanism that can surpass these limitations or improve tolerance can bring a revolutionary shift in industrial applications.

In search of the counterparts of conventional thermocouples or strain gauges, fiber optic sensors have gained popularity due to their unique advantages such as small size, light weight, immunity to electromagnetic interference, harsh environment compatibility, and multiplexing capacity [1, 2]. Therefore, these sensors have been extensively studied for measurement of a wide range of physical and chemical parameters, including temperature, pressure, strain, displacement, salinity, and corrosion in various applications [3, 4, 5, 6]. In this dissertation, we have developed several methods to measure temperature with high accuracy and free from cross-strain sensitivity by using Fiber-optic Fabry-Pérot (FP) interferometer sensor. We also introduced a novel method to measure strain and temperature simultaneously using a cascaded Fiber Bragg Gratings (FBG)- silicon FP interferometer.

For the last three decades, various techniques have been developed regarding fiber optic temperature sensors such as fiber-Bragg grating (FBG) based sensors [7], interferometer-based sensors [8, 9, 10], waveguide coupling devices using surface plasmon resonance [11], Brillouin frequency shift [12, 13], fiber loop rinrgdown [14, 15] or fiber ring laser demodulation [16]. Among these, temperature sensors based on Fabry-Pérot (FP) interferometers have proved to be an attractive option because of their additional advantages of simple structure and easy fabrication. Also, their short

cavity length or propagation in air can mitigate the issue with optical power fading which usually occurs with Mach–Zehnder and Michelson interferometers due to polarization and birefringence of optical fiber [17].

The Fabry-Pérot interferometer was first introduced in 1897 by two French physicists Charles Fabry and Alfred Pérot [18]. It consists of two highly reflective parallel plates or mirrors (known as 'etalon'). Exploiting the high reflectivity of the etalon mirrors, the successive multiple reflections of light waves get interfered between the mirror and diminish very slowly in intensity and form very narrow, sharp fringes. This principle was introduced in optical fiber sensors around 1980s by many scientists and engineers through ongoing research and innovation in the field of fiber-optics.

In conventional fiber optic FP interferometers, one of the cavity mirrors is typically formed by a cleaved single-mode fiber (SMF), while the other mirror is parallel to the fiber end-face, which can be a thin film, capillary tube, or another section of the fiber end-face. After light is emitted from the core of the fiber, it travels through the fiber's end-face and interacts with the mirror, resulting in multiple reflections and interference. Figure 1.1 demonstrates the basic configuration of a Fabry–Pérot interferometer sensor based on the Fresnel reflection principle, which governs the reflection at the interface between two media with different refractive indices (RI). For example, as shown in Figure 1.1, the reflection of light happened on two surfaces: the fiber-silicon and silicon-air, where R_1 and R_2 are the reflection coefficients for these two surfaces, respectively. Consequently, R_1 and R_1 can be determined as follows [19],

$$R_1 = \frac{(n_f - n)^2}{(n_f + n)^2} \tag{1.1}$$

$$R_2 = \frac{(n - n_{air})^2}{(n + n_{air})^2} \tag{1.2}$$

where, n_f , n, and n_{air} are the RI of the fiber, silicon, and air, respectively. Within the fiber core, all reflected light waves experience interference, resulting in a complex amplitude expressed as,

$$E_r = \sqrt{R_1} E_i e^{i\pi} + (1 - A_1)(1 - R_1)(1 - \alpha) \times \sqrt{R_2} E_i \exp(-j2\beta l)$$
 (1.3)

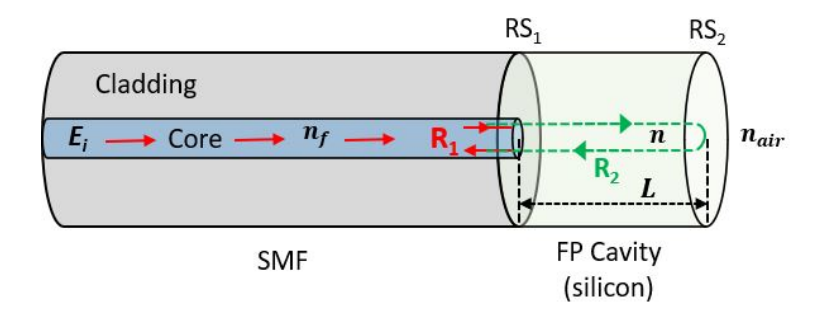


Figure 1.1 Schematic of a typical FP interferometer sensor.

where E_i is the initial reflection amplitude, A_1 is the transmission loss factor, β is the propagation constant in cavity, and α is the loss factor of the cavity.

Normalized reflection spectrum,

$$R_{FP}(\lambda) = \left| \frac{E_r}{E_i} \right| = R_1 + (1 - A_1)^2 (1 - R_1)^2 (1 - \alpha)^2 R_2 - 2\sqrt{R_1 R_2} (1 - A_1) (1 - R_1) (1 - \alpha) \cos \phi$$
 (1.4)

where ϕ is the corresponding phase difference, which can be expressed as

$$\phi = \frac{4\pi nl}{\lambda} \tag{1.5}$$

where n represents the refractive index of the medium between the two cavity mirrors, L denotes the separation distance between the two mirrors, and λ signifies the wavelength of the incident light wave. When this phase difference meets a periodic condition, i.e., $\phi = 4\pi nL/\lambda = 2m\pi$, the interference of the reflected light results in destructive interference, where m represents the order of resonant wavelengths. Hence, Eq. 1.5 can be written as,

$$\lambda_n = \frac{2nL}{m} \tag{1.6}$$

This λ_n is the periodic valley wavelength, which is modulated by surrounding perturbations such as change in temperature, pressure, strain, etc. More specifically, in case of temperature change, the sensing material's refractive index n, and the characteristic length L are changed with temperature through thermo-optic effect, and thermal expansion, respectively.

Figure 1.2 shows a schematic diagram of a typical interrogation setup for a fiber-optic sensor. White light is coupled to the core of a single-mode fiber from a broadband light source and

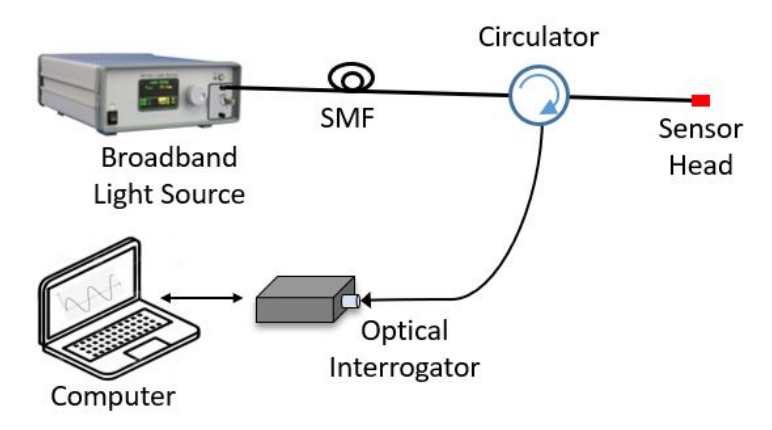


Figure 1.2 Schematic of a typical fiber optic sensor interrogation setup.

transferred to the sensor head, where it gets reflected multiple times depending on the sensor configuration. These reflected light waves are directed to a high-speed spectrometer or interrogator through a circulator. We have used average wavelength tracking method for signal demodulation, which is described in the later chapters in details.

1.2 Motivation of this Work

High-accuracy temperature and strain measurements have become a prerequisite for operation of many modern industries. Especially in energy systems, it is very crucial to ensure the sustainability of steam cycles, reduction in greenhouse gas emissions, and increase in power plant efficiency [20, 21, 22]. For example, in coal-fired power plants, an increase in the live steam temperature by 1 °C can increase the efficiency by 0.02% [20], and a 1% increase in energy efficiency leads to a decrease in greenhouse gas emissions by 1.3% [21]. However an increase in the steam temperature above 600–620 °C will require special alloy materials [22], and hence increase the specific cost of the power plant by 5–10%. Similarly, inaccurate strain measurement can result in structural failures and safety hazards. Usually, thermocouples are used to measure temperature in industrial applications, which have various standards. According to International Electrotechnical Commission (IEC) standard 60584-1, thermocouples with tolerance of ±1.5 °C or ±0.25 % of the measured temperature are classified as Class 1 [23]. But even the standard class thermocouples also possess several drawbacks, including large size, vulnerability to corrosion, tendency to drift over time, and susceptibility to electromagnetic interference, which reduce their usefulness in these

applications [24]. For strain measurement, various techniques are applied including strain gauge, load cell, piezoelectric transducer, etc [25]. However, these have limitations of complex installation and calibration, large size, and dynamic measurement. In search of the counterpart of these bulky thermocouples and strain gauges, researchers have found fiber optic sensors quite useful due to their unique advantages, such as small size, light weight, immunity to electromagnetic interference, multiplexing capability, and harsh environments compatibility [1, 2].

As stated earlier, researchers have developed various techniques regarding fiber optic sensors, including fiber Bragg gratings (FBG) [26, 27], interferometer based sensors [10, 28, 29, 30, 31, 32, 33, 34, 35, 36, 37, 38, 39, 40, 41, 42], surface plasmon resonance [43, 44, 45], ring resonator [46], etc. Among these, Fabry-Pérot interferometer sensor has drawn attention to many researchers for its additional advantages. The research in this dissertation is also based on this FP interferometer, whose theory is described in the previous section. Nowadays, different types of FP interferometers have been deployed in terms of composition and fabrication process. For example, interferometers can belong to the following types (a) fiber-tip: SMF-microfiber [28], SMF-polyvinyl alcohol [29]; (b) with diaphragm: FBGgraphene [10, 30], MMF-silicon [31], FBG-fused silica [32]; (c) without diaphragm [33]; (d) polymer materials [34]; (e) inline microcavities [35, 36]; (f) multiplexed sensors [37]; (g) microcantilever [38], (h) polished materials [39], (i) modified fibers (panda fibers [40], multicore fiber [41], tapered fiber [42]) and so on.

The working principle of most of these sensors relies on spectral modulation resulting from the dependency of their optical path length on surrounding perturbations. More specifically, sensing material's refractive index n, and the characteristic length l (grating period for FBG, cavity length for FPI etc.) are dependent on temperature, which is measured through thermo-optic coefficient (TOC) and thermal expansion coefficient (TEC), respectively. While this dependency allows for temperature measurement within a specific range, it is susceptible to interference from cross-sensitivity to other perturbations, such as strain, pressure, and more. For example, a FBG exhibits temperature sensitivity of 10 pm/°C, whereas its strain sensitivity is 1 pm/ $\mu\epsilon$ [7]. This cross-sensitivity can introduce measurement errors, particularly in harsh environments with sig-

nificant stress. To overcome this drawback, some studies implement techniques for simultaneous measurement of temperature and strain or other perturbations [10, 36, 47]. But these sensors mostly require calibration due to their inherent FP cavity length change during interrogation. Also, for multiple parameter measurement, many of these works utilize an FBG along with FP Interferometer sensor, where the lower sensitivity of FBG to temperature (~10 pm/°C) affects the accuracy at high temperature measurement [10, 47]. Many researchers have used cavities formed by a tip composed of graphene or other materials as diaphragm or cantilever. These materials have large thermal expansion coefficients (TEC) and thermo-optic coefficient (TOC) compared to their glass material counterparts, resulting in higher temperature resolution. But the fabrication process often requires complex MEMS techniques [38, 31], chemical processing [10, 29, 30], or high-power laser ablation [32], which is expensive, time-consuming, and lacking in reproducibility. Also, these sensors show nonlinearity at high temperature because the composite structure's TOC becomes a complex function of temperature, resulting in a limited operation range [34]. Even if we consider no external strain is applied, many fiber optic sensors exhibit a shift in wavelength for long-term exposure to high temperature due to dopant diffusion [48], induced residual stress for frozen-in viscoelasticity [49], devitrification (crystallization) of the glass [50], etc. Researchers invented complicated annealing processes to slow down this drift to achieve stability [51]. Nevertheless, the fiber's mechanical strength experiences a substantial decline, making it unsuitable for practical applications.

Another limitation of the concurrent fiber optic sensor research is the signal demodulation. These FP interferometer sensors [52, 53, 54] are mainly based on dual cavity, where the composite wavelength signal is demodulated by using FFT with various algorithms such as white light interferometry [55], wavelet phase extraction [56], wavelet transform and polarized low-coherence interferometry [57], and coarse spectrum [58]. Most of them provide \sim 10 nm accuracy in cavity length measurement, which can result in \pm 5 °C error in temperature measurement at around 800 °C. Additionally, these methods have drawbacks, e.g., limited cavity length range, susceptibility to noise, and slow demodulation speed.

To overcome these drawbacks, we have demonstrated a fiber optic temperature sensor based on air-filled FP cavity with variable and controlled pressure. To perform the measurement, the FP reflection spectrum was recorded when the air pressure was varied. Utilizing the fact that the difference of air refractive index and unity is linearly proportional to the pressure and inversely proportional to the absolute temperature, absolute temperature can be extracted from the slope of the spectral shift vs. pressure. This measurement method renders many advantages compared to conventional fiber-optic sensors. Firstly, the working principle dictates that the sensor has zero strain cross-sensitivity over a broad temperature range. Since we measured wavelengths inside an enclosed setup with identical pressure, the change in cavity length due to strain or other perturbation does not affect the temperature measurement. Secondly, the use of air as the sensing material eliminates drifts from material degradation often encountered by solid materials at high temperature. Thirdly, the sensor's fabrication process is very straightforward through standard splicing technology. Fourthly, we have used average wavelength tracking for signal demodulation, which effectively reduces wavelength noise by taking multiple valleys.

We have proposed a couple of approaches based on this air-filled FP cavity interferometer sensor. The first approach utilizes a miniaturized electronic pump to pass air through the holes of the side-hole fiber to change the FP cavity pressure. Temperature is measured by obtaining the two different wavelengths corresponding to the two pressures. The instrumentation is designed to be controlled electronically and miniaturized in size to facilitate a fast and practical temperature measurement. The second approach utilizes two FP interferometer sensors in the setup, which has enabled to measure temperature without the knowledge of the optical property of gas (α) or the requirement of using pressure transducer to read pressure, resulting in simpler and cost-effective instrumentation. We experimentally verified our proposed method up to a range from room temperature to 800 °C and theoretically analyzed the effect of wavelength resolution (noise) on temperature measurement. The results showed a very linear and high-resolution sensor for both methods.

In addition, we have also demonstrated a novel method to measure both temperature and strain simultaneously by cascading a fiber Bragg grating to a silicon pillar to form the FP cavity. This

method implies the discriminative sensitivity of both the FBG and FP interferometer to the two measurands. Thanks to the high thermal expansion and thermo-optic coefficient of silicon, the temperature sensitivity of the FP interferometer is obtained 89 pm/°C, and the FBG is used to measure strain, compensating the shift induced by thermal expansion of the host material. This is described in detail later in Chapter 4. Finally, we have a short discussion of future work and make a summary of this dissertation.

1.3 Outline of Dissertation

This dissertation is organized into five chapters, as follows:

Chapter 1 contains the background and the motivation behind this work through a thorough literature review of concurrent research on fiber-optic sensors.

Chapter 2 introduces our novel method of temperature measurement using air-filled Fabry-Pérot cavity with variable pressure. This chapter describes the working principle, fabrication method, experimental setup, and characterization of the sensor for temperature measurement. This chapter also includes a theoretical analysis of the impact of key parameters such as wavelength resolution and pressure fluctuation on temperature measurement.

Chapter 3 describes a modified approach to measure temperature using a pair of FP interferometers, with identical but variable FP cavity pressure. This method facilitates the instrumentation by replacing the pressure sensing device with an additional sensor. We have also performed a theoretical analysis on temperature resolution due to the wavelength noise. The chapter compares the pros and cons of these two methods at the end.

Chapter 4 focuses on the development of cascaded FBG-silicon FPI sensor to measure temperature and strain simultaneously. We have discussed the fabrication process, working principle of this sensor, experimental setup with results and discussion.

Chapter 5 briefly summarizes this research work and concludes the dissertation. This chapter discusses our research findings and the limitations of this work. It also mentions the possible future directions of this work for further development.

CHAPTER 2

TEMPERATURE MEASUREMENT USING AIR-FILLED FABRY-PÉROT CAVITY WITH VARIABLE PRESSURE

2.1 Introduction

Numerous research studies have been conducted regarding fiber optic sensors for temperature measurement in recent times. The main challenges with these sensors are complex fabrication method, sensor's drift at elevated temperatures, cross-strain (or pressure) sensitivity, calibration requirements, and long-term instability. Researchers have invented various configurations of sensors to overcome these drawbacks. We have described the concurrent research trends and their limitations in the previous chapter.

To overcome these drawbacks, our previous work [59] proposed and demonstrated a fiber optic temperature sensor based on air-filled FP cavity with variable and controlled pressure. To perform the measurement, the FP reflection spectrum was recorded when the air pressure was varied. Utilizing the fact that the difference of air refractive index and unity is linearly proportional to the pressure and inversely proportional to the absolute temperature, absolute temperature can be extracted from the slope of the spectral shift vs. pressure. The measurement principle dictates that the sensor has zero strain cross-sensitivity over a broad temperature range, and the use of air as the sensing material eliminates drifts from material degradation often encountered by solid materials at high temperatures. However, the system demonstrated in our previous work has a few drawbacks that limit its usefulness in practical applications. To achieve a temperature reading, the slope of the spectral shift vs. pressure was obtained using curve fitting by measuring the reflection spectrum at multiple air pressure levels over a large pressure range of 1500 psi using a manual air pressure pump. Generating such a high air pressure level is not a trivial task, and often requires expensive and bulky instrumentation, as well as long pumping time.

In this chapter, we have reported our theoretical and experimental work for further development of the fiber optic temperature sensor toward practical applications. The sensor head is fabricated by splicing a fused-silica capillary tube with a single-mode fiber (SMF) on one end and a side-hole fiber

on the other end. The pressure of the cavity is changed by passing air through the holes of the side-hole fiber. Instead of using very high pressure and bulky instruments as in our previous work [59], we used miniaturized instruments with lower pressure $(100\,\mathrm{psi}_g)$. Each temperature reading is obtained by recording the spectrum at two pressure levels. This makes the sensor acquisition system compact, portable, fast, and electronically controlled. We developed a model and theoretically analyzed the effect of key system parameters, including the wavelength resolution in the spectral shift and the pressure stability on system performance in terms of temperature measurement resolution and stability. In the experiment, our sensor shows high wavelength resolution ($<0.2\,\mathrm{pm}$), linear response, reduced strain cross-sensitivity, and high accuracy with repeatability for a broad operation range (room temperature to over $800\,^{\circ}\mathrm{C}$). Most of the contents of this chapter are published in MDPI Sensors journal [60] and reproduced in this dissertation with permission from the publishers – MDPI.

2.2 Sensor Fabrication

Figure 2.1(a) shows the schematic of the sensor head, which consists of a single mode fiber (SMF), a fused-silica capillary tube, and a side-hole fiber of identical diameter (125 μm). The silica tube has a hollow of 75 μm diameter inside it. The side hole fiber has two holes of 20 μm diameter along the cladding. Figure 2.1(b) and Figure 2.1(c) show their cross-sectional view of the silica tube and side-hole fiber, respectively. Some deformity is seen in the contact edge of the cleaver blade.

For fabrication, we spliced the SMF with a silica tube by a fusion splicer (Sumitomo Type-36) using optimized splicing parameters (see Table 2.1). We cleaved the end of the silica tube and spliced it again with the side-hole fiber. The length of the silica tube is kept $\sim 95 \, \mu m$, which acts as the enclosed FP cavity. Finally, we cleave the side-hole fiber end with 8° angle keeping appropriate length. The holes in the side-hole fiber are employed as venting holes for pressurizing the FP cavity. The 8° end face of the side-hole fiber effectively eliminates the back reflection from that end face to the SMF. Figure 2.2 shows the fabrication process steps.

Figure 2.3(a) shows the longitudinal view of the fabricated sensor. The reflection spectrum of

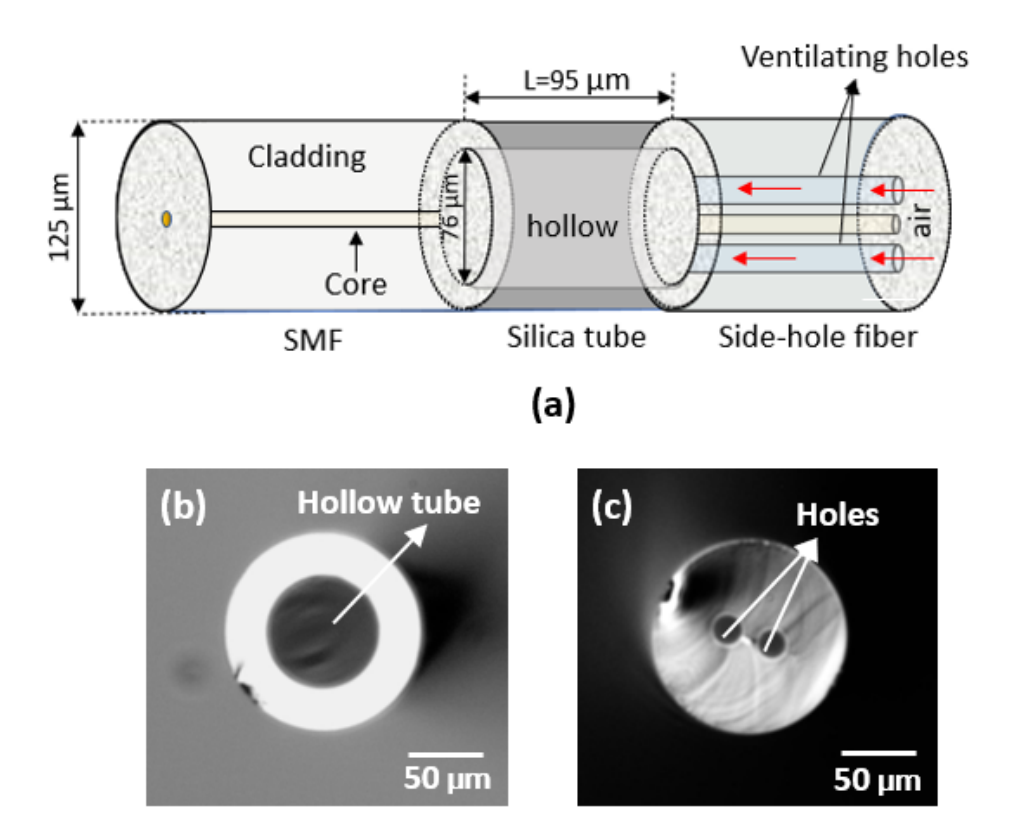


Figure 2.1 (a) Schematic of the sensor; (b) and (c) cross-section of silica tube and side-hole fiber, respectively.

Table 2.1 Optimized splicing parameter for fabrication

Splicing Parameter	Value
Arc duration	1.50 s
Prefusion	0.10 s
Arc gap	10.0 μm
Overlap	5.0 μm
Arc power	20 dB

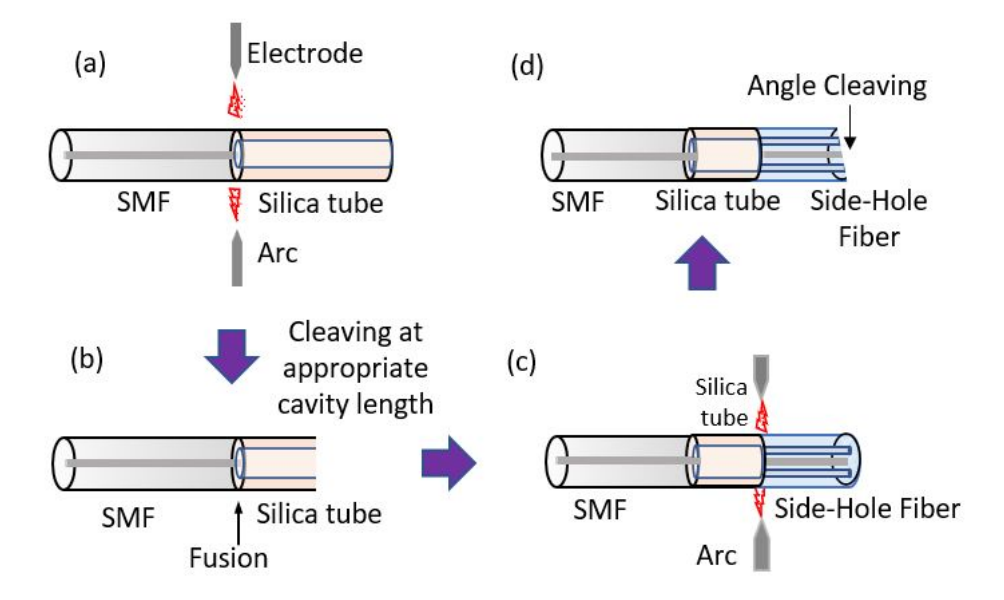


Figure 2.2 Fabrication process of the Fabry-Pérot fiber-optic interferometer sensor.

the sensor at ambient temperature and pressure is shown in Figure 2.3(b). The spectrum shows that the sensor has a good visibility of >18 dB and the free spectral range (FSR) is around 12.5 nm, corresponding to a cavity length of \sim 96 μ m, consistent with the silica tube length obtained from the microscope image of the sensor.

2.3 Principle of Operation

The wavelength of a fringe valley of an FPI sensor's reflection spectrum, λ , is given by:

$$\lambda = \frac{2nl}{m} \tag{2.1}$$

where n is the refractive index of FP cavity material, l, is the cavity length, and m is the order number of the fringe valley. We used air to fill the FP cavity. It is known that the difference between refractive index of many gases, including the air, and unity (n-1) is, to a good degree of accuracy, proportional to pressure P, and inversely proportional to absolute temperature T (in the unit of Kelvin), or

$$n - 1 = \frac{\alpha P}{T} \tag{2.2}$$

where α is a constant characterizing the optical property of the gas and is stable under high

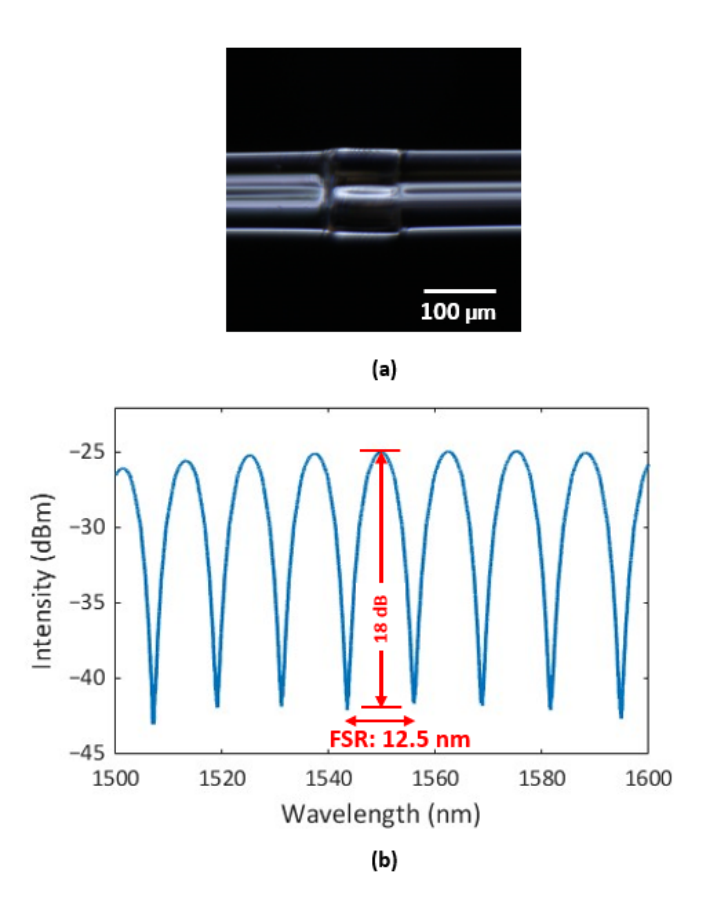


Figure 2.3 (a) Microscopic longitudinal view of the fabricated sensor; (b) reflection spectrum of the sensor at ambient temperature and pressure.

temperature. Combining Eq. 2.1 and Eq. 2.2,

$$\lambda = \frac{2l}{m} \left(\frac{\alpha}{T} P + 1 \right) \tag{2.3}$$

For temperature measurement, the pressure in FP cavity P is varied and the sensor spectrum is measured to determine wavelengths of the fringe valleys as a function of pressure P. Specifically, assuming we have obtained the wavelength locations of a fringe valley, λ_1 and λ_2 , at two different pressure levels of P_1 and P_2 , respectively, it follows,

$$\lambda_1 = \frac{2l}{m} \left(\frac{\alpha}{T} P_1 + 1 \right) \tag{2.4}$$

$$\lambda_2 = \frac{2l}{m} \left(\frac{\alpha}{T} P_2 + 1 \right) \tag{2.5}$$

Solving Eq. 2.4 and Eq. 2.5, we obtain an expression for the temperature independent of the cavity length, l, as

$$T = \frac{\alpha(P_2\lambda_1 - P_1\lambda_2)}{\lambda_2 - \lambda_1} \tag{2.6}$$

Note that, in deriving Eq. 2.6, we assumed that the cavity length remains unchanged when the pressure is varied, so the l (as well as the order number m) in Eq. 2.4 and 2.5 can be cancelled out. Eq. 2.6 shows that the absolute temperature T can be deduced from the two different pressure levels, their corresponding FP interferometric fringe wavelengths, and the parameter α , which is determined by the intrinsic gas property independent of cavity length. Therefore, this method of temperature measurement is not affected by the changes in the cavity length due to thermal expansion or strain. In addition, as gas is generally a stable state at high temperature, α is also stable and the temperature sensor is expected to have little drift.

2.4 Noise Analysis

Eq. 2.6 indicates that the measurement resolution and accuracy are determined by the resolution and accuracy in determining the fringe valley wavelength and pressure. We have theoretically analyzed the effect of the parameters on the system performance. In practice, the system performance would benefit from a large difference between P_2 and P_1 . Therefore, we can assume $P_2 \gg P_1$, which yields,

$$T \approx \frac{\alpha \lambda_1 P_2}{\lambda_2 - \lambda_1} \tag{2.7}$$

Differentiating Eq. 2.7 with respect to P_2 , we get the resolution (standard deviation) of the temperature measurement, δT , in relation to the resolution of the pressure determination, δP_2 ,

$$\frac{\delta T}{T} = \frac{\delta P_2}{P_2} \tag{2.8}$$

Now, differentiating Eq. 2.7 with respect to $\lambda_2 - \lambda_1$ and after some simplification,

$$\frac{\delta T}{T} = \frac{\sqrt{2}\delta\lambda}{\lambda_2 - \lambda_1} \tag{2.9}$$

where $\delta\lambda$ is the resolution of wavelength determination of the fringe valley (which is assumed to be equal for both pressure levels). Eq. 2.8 and Eq. 2.9 show the effect of pressure and wavelength

resolutions on temperature measurement resolution, respectively. Since these measurements are independent to each other, we can add both to calculate the resolution of the sensor:

$$\frac{\delta T}{T} = \frac{\delta P_2}{P_2} + \frac{\sqrt{2}\delta\lambda}{\lambda_2 - \lambda_1} \tag{2.10}$$

Note that, $\lambda_2 - \lambda_1$, the spectral shift as the pressure changes from P_1 to P_2 , is also a function of the temperature. Using Eq. 2.4, Eq. 2.5, and Eq. 2.1 and the approximation that $n \approx 1$ for air, as well as the assumption that $P_2 \gg P_1$, we obtain $\lambda_2 - \lambda_1 \approx (\alpha \lambda_1 P_2)/T$. Then we can express Eq. 2.10 as

$$\frac{\delta T}{T} = \frac{\delta P_2}{P_2} + \left(\frac{\sqrt{2}}{n_2 - 1}\right) \left(\frac{\delta \lambda}{\lambda_1}\right) \tag{2.11}$$

where n_2 is the air refractive index at pressure P_2 and temperature T. From Eq. 2.11, it reveals that the wavelength noise is likely to be the dominant noise contributor to the system noise because n_2 is a number close to 1. For example, for dry air at 100 psi and 15°C, it is estimated that $n_2 - 1 \approx 0.002$ at 1550 nm using the value for the air refractive at the standard pressure and the same temperature [61]. The wavelength noise is amplified by 500 times when it is transferred to the measurement noise of temperature. In this work, we used an average wavelength tracking method [62] exploiting multiple valleys in the spectrum to measure λ for varying pressure. This method helps to alleviate the wavelength noise and calculate the sensor resolution more precisely. In addition, the noise contribution from the wavelength noise is proportional to the absolute temperature and inversely proportional to pressure. It means, for a given sensor system with fixed pressure variation, the noise would be dependent on the measurand (temperature) and larger at higher temperature levels.

2.5 Experimental Setup

We developed a computer-controlled sensor acquisition system with portable and miniaturized instruments. Figure 2.4 shows the schematic of the system. To measure the sensor's wavelength spectrum, we used a fiber optic sensor interrogator (Model: Hyperion si-155, manufacturer: Luna Innovations, VA, USA) with 1 pm accuracy. We used a thermal furnace to increase the temperature for sensor characterization. The pressure in the FP cavity is changed by a miniaturized electronic

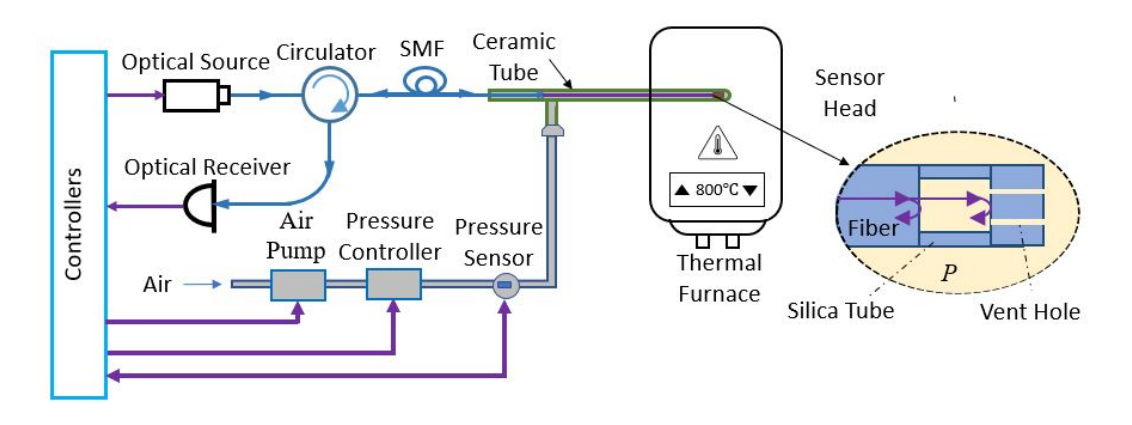


Figure 2.4 Schematics of the fiber-optic temperature sensor system.

pressure pump (model: H1R-080P24HV-02, Manufacturer: Parker Hannifin, NH, USA). For our experiment, we chose two different pressure levels of 0 psi $_g$ and 100 psi $_g$ (or 690 kPa) as P_1 and P_2 , respectively. We used an electrical shut-off valve to stabilize the pressure fluctuations while taking the readings. To read the pressure, we used a precision pressure transducer with 0.020% full-scale accuracy. The pump, valve, and pressure transducer are miniaturized in size (longest dimension is <4.3 inch) and electronically controlled. We used a programmable power supply to run these instruments. The whole setup is programmed in MATLAB code and the wavelength and pressure data are stored simultaneously in the control unit (computer). It takes less than one minute to pressurize the chamber from 0 psi $_g$ to 100 psi $_g$ and the pressure becomes stable very quickly after shutting the valve off. We used an alumina ceramic tube to house the sensor in a pneumatic setup to prevent any air leak. Additionally, ceramic tubes have high melting temperature (over 2500 °C) and flexural strength (~54,000 psi), which makes it suitable for high-temperature applications. As described in the theory section, temperature can be measured by taking the data of two pressure levels P_1 and P_2 and their corresponding wavelengths λ_1 and λ_2 . Figure 2.5 shows the flowchart of the integrated computer-controlled temperature measurement system.

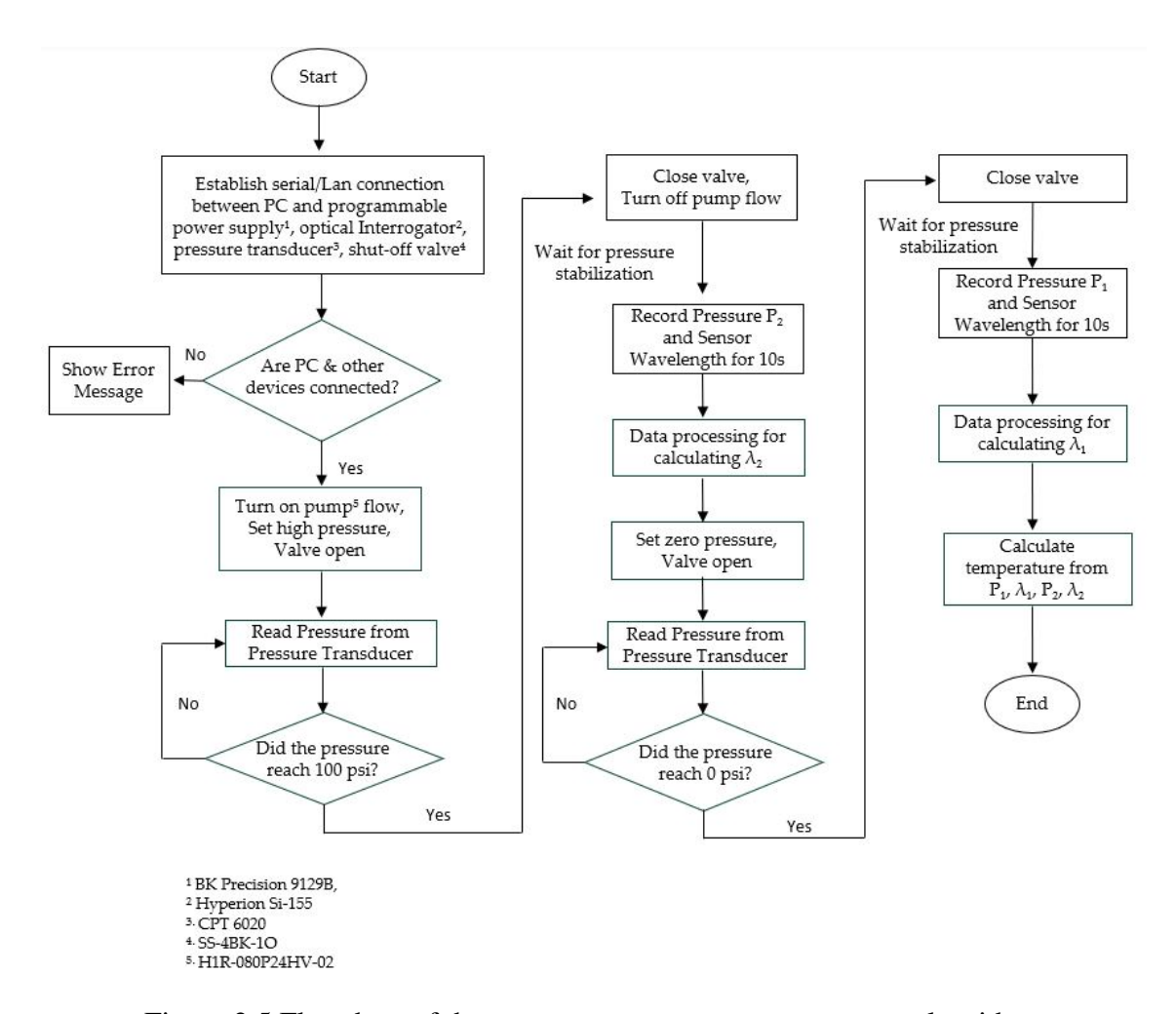


Figure 2.5 Flowchart of the temperature measurement system algorithm.

2.6 Wavelength Demodulation

For wavelength demodulation from the spectrometer, we used 'average wavelength tracking method' originally developed in [62]. In this method, we first set a threshold to define valleys. These valleys are processed with Gaussian curve fitting and the valley wavelength location is found by maxima of a second-order polynomial. Figure 2.6(a) shows a typical reflection spectrum of a FP sensor where we define five valleys (shown by blue data) for a specific wavelength range by a threshold line, and Figure 2.6(b) shows the curve fitting for those valleys to demodulate wavelength location. This method eliminates the wavelength noise caused by spurious jumps of any specific valley by a factor of \sqrt{M} , where M is the number of valleys (or peaks) used to calculate average wavelength [62].

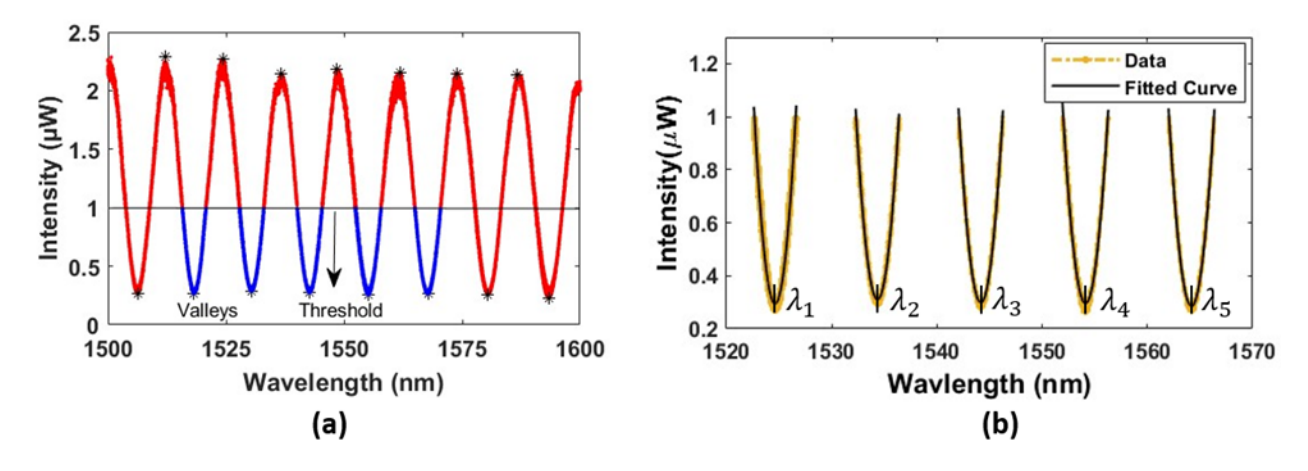


Figure 2.6 (a) Reflection spectrum of an FP sensor with a threshold line to define valleys, (b) curve fitting for wavelength detection.

2.7 Sensor Characterization

2.7.1 Spectral Shift with Pressure

Using the above setup, we increased the pressure from 0 psi_g to 100 psi_g or 690 kPa (pressure is relative to gauge, not absolute pressure) to see the spectral shift of the sensor. It is seen that the interferometric fringes shift toward the higher wavelength with increase in pressure. This shift is reduced at high temperature. For example, the spectral shift with pressure decreases from 4.01 pm/kPa to 1.17 pm/kPa when the temperature is increased from room temperature (25 °C) to 800 °C (see Figure 2.7). To see how the spectral shift is affected at different temperatures, we increased

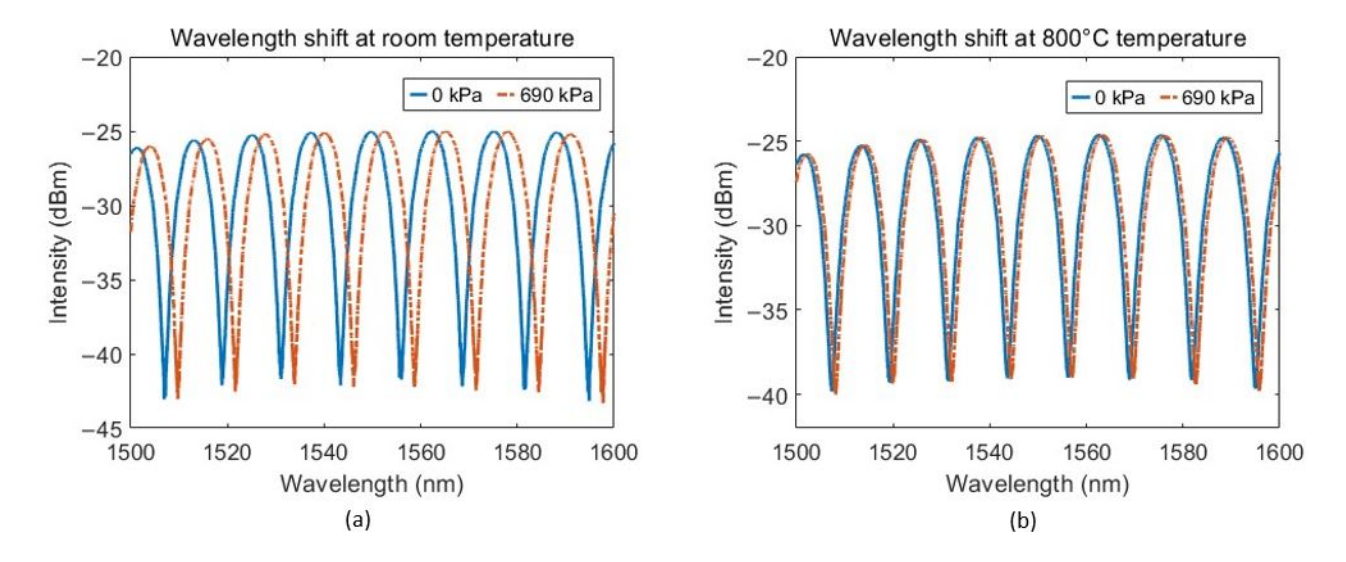


Figure 2.7 Reflection spectra for two different pressure levels at (a) room temperature and (b) 800 °C temperature.

temperature from 25 °C to 800 °C with step size of 25 °C and recorded the wavelength shift for 690 kPa pressure change. Figure 2.8 shows the graph of spectral shift per unit pressure change $(\Delta \lambda/\Delta P)$ vs. absolute temperature (T), where $\Delta \lambda$ is the spectral shift for a change in pressure ΔP . This curve is fitted with the theoretical curve. Subtracting Eq. 2.4 from Eq. 2.5 yields

$$\frac{\lambda_2 - \lambda_1}{P_2 - P_1} = \frac{\Delta \lambda}{\Delta P} = \frac{2l}{m} \alpha \approx \frac{\lambda \alpha}{T} = \frac{A}{T}$$
 (2.12)

Here, $A = \lambda \alpha$ and λ is the central wavelength, which is used for cavity length calculation. Fitting the experimental results with Eq. (2.12) leads to the fitting parameter, A = 1240 pm-K/kPa and shows a good agreement between the fitting curve and the experimental results, as shown in Figure 2.8, indicative of the validness of the theoretical model. This also experimentally validated that the gas material properties α have negligible effects over this broad temperature range, and can be considered as constants in our proposed model.

2.7.2 Linearity Test

To validate our proposed temperature measurement method according to Eq. 2.6, we have calculated $S = (P_2\lambda_1 - P_1\lambda_2)/(\lambda_2 - \lambda_1)$ for different temperatures ranging from 25 °C to 800 °C.

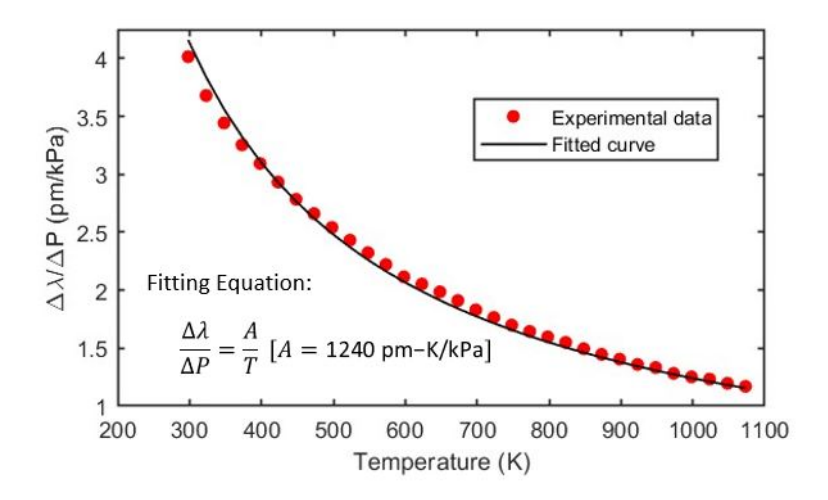


Figure 2.8 Spectral shift with pressure at different temperatures.

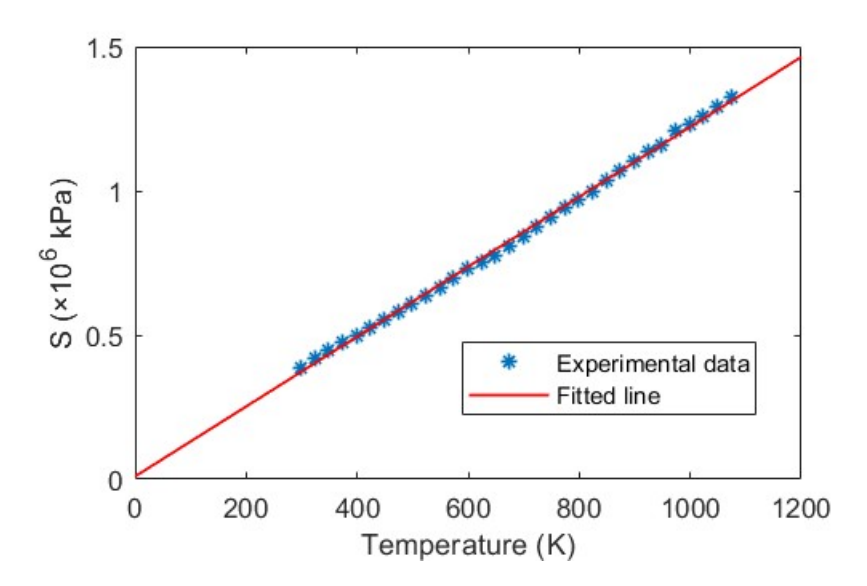


Figure 2.9 Linear relationship between temperature *T* and *S*.

Figure 2.9 shows the linear relationship between the absolute temperature T (in K unit) and S (in kPa). The R-square of the linear fitting coefficient is found 0.9986. This shows that the sensor is very linear even at a very high temperature (over 800 °C). The good agreement also indicates the validity of the theoretical model. From Eq. 2.6, the value of the gas (air) constant, α is found 8.2515×10^{-4} K/kPa (or 0.00535 K/psi) which matches with our previous work [59]. So, this temperature measurement method requires no calibration, even if the sensor's cavity length is different.

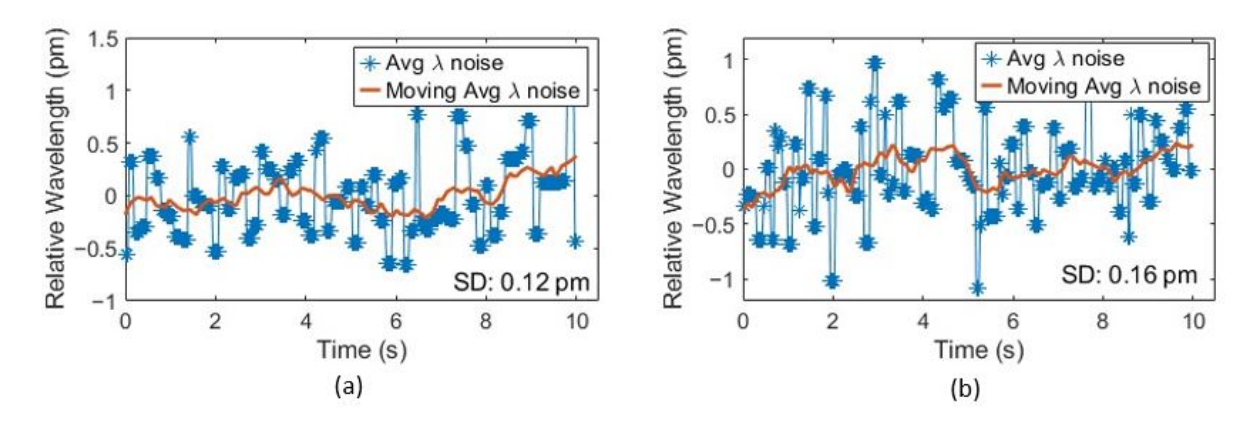


Figure 2.10 Sensor wavelength resolution at room temperature for (a) 0 psi_g and (b) 100 psi_g pressure.

2.7.3 Wavelength Resolution

Wavelength resolution is defined as the variation of fringe wavelength over a small period of time. It is calculated by taking the standard deviation of the moving average of multiple valley wavelengths. For this, we have recorded the reflection spectrum from the fiber optic sensor interrogator for 10 seconds of duration at 1 kHz scanning rate. Instead of using only one fringe valley as our previous work [59], we have taken the arithmetic average of the first seven valleys in the range of 1500-1600 nm to find the parameter $\bar{\lambda}$ for a specific temperature and pressure. Since we recorded data for 10s of duration for each measurement, the moving average of $\bar{\lambda}$ is taken to calculate the wavelength λ to be used in Eq. 2.6. Figure 2.10 shows that the sensor resolution at ambient room temperature (25 °C) is 0.12 pm and 0.16 pm for two pressure levels, 0 and 100 psi, respectively. To measure the sensor resolution at high temperature, we continued the same test from 25 °C to 800 °C. Figure 2.11 shows the wavelength resolution of the sensor at different temperatures. It is seen that the wavelength resolution is found in the range of 0.07-0.2 pm even with this broad operation range. According to Eq. 2.9, the accuracy for temperature measurement with this resolution is within ± 0.32 °C, theoretically.

2.7.4 Pressure Fluctuation

As we have described earlier, pressure stability is another prerequisite for our sensor's accurate temperature measurement. Theoretically, the fluctuation in high pressure P_2 , (for our case, 100

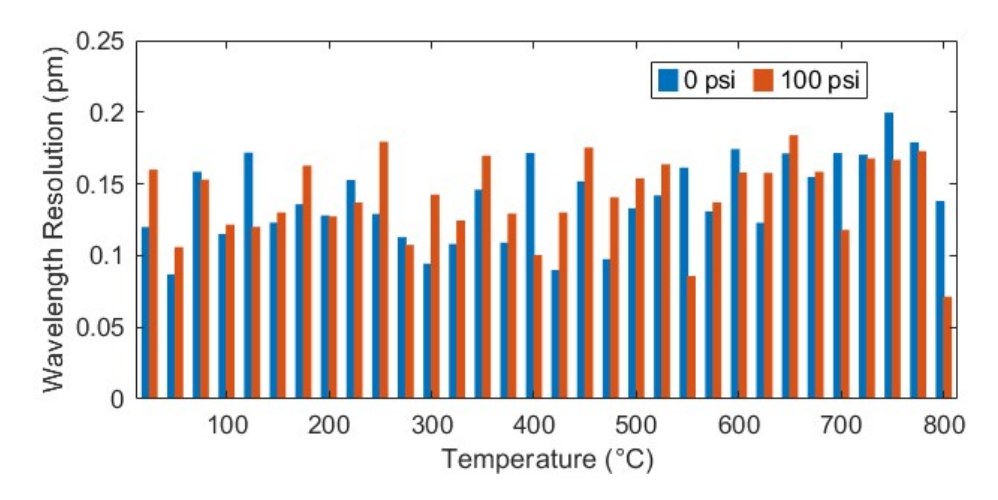


Figure 2.11 Sensor wavelength resolution for two different pressure levels at each measurement.

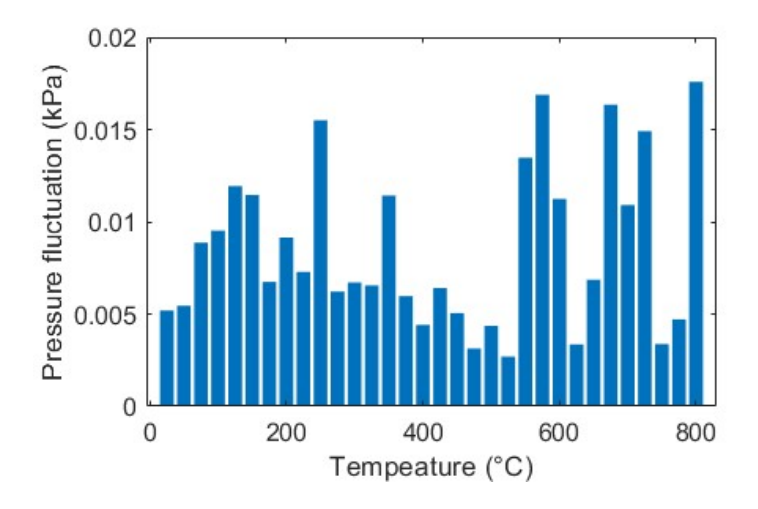


Figure 2.12 Pressure fluctuation δP_2 at each measurement.

psi_g) can cause the temperature measurement error by $\delta P_2/P_2$ (Eq. 2.8). We measured the pressure of the system by a precision pressure transducer (CPT6020) while doing the wavelength resolution test. Figure 2.12 shows the pressure fluctuations δP_2 for different measurements. It is seen that the system is quite stable to limit the pressure fluctuations in the range of 0.0027–0.0176 kPa. With this setup, the temperature measurement error due to this pressure fluctuation is negligible (< 0.035°C).

2.7.5 Temperature Resolution

We can theoretically measure the temperature resolution δT from the two key parameters of this system- wavelength resolution $\delta \lambda$ and pressure fluctuation δP following Eq. 2.11. Since the

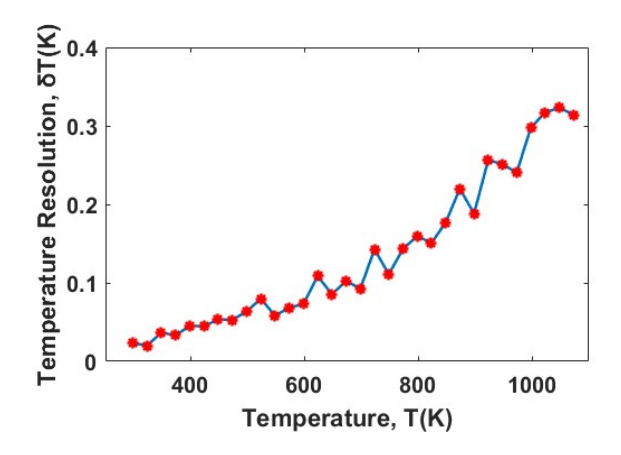


Figure 2.13 Temperature resolution δT obtained for various temperature T.

value of $\delta\lambda$ and δP can be obtained experimentally as mentioned in the previous subsections, we can obtain temperature resolution for our experimental range of up to 800 °C. From Figure 2.13, it is seen that the maximum temperature resolution (noise) can be reached up to ± 0.32 °C (or K), mostly contributed by the wavelength noise.

2.7.6 Repeatability Test

To investigate the repeatability of our fabricated sensor, we have taken a thermal-cycle test where we repeatedly heated the sensor from room temperature to 800 °C and again cool down the sensor to room temperature. In each cycle, we measured the room temperature and high temperature according to Eq. 2.6 by using the empirical value of gas constant $\alpha = 8.2515 \times 10^{-4}$ K/kPa. We also measured the temperature each time with a reference thermometer (Pt100) with a high accuracy of ± 0.1 °C for comparison. Table 2.2 shows that measured temperature by our sensor matches well to the reference thermometer to a high degree of accuracy. At room temperature the difference is ~ 0.5 °C, whereas at high temperature of 800 °C, it increased to ~ 3 °C. This can be explained by the fact that at this high temperature, the furnace has limitation of accuracy (± 3 °C) and temperature uniformity (± 4.8 °C), and the accuracy of the reference thermocouple can also deteriorate. The thermal cycle test proves that our fabricated sensor's accuracy is repeatable even after heating it to a very high temperature several times. The excellent accuracy from the thermal cycle test is also proof of the validity of the theoretical model of the sensor operation.

Table 2.2 Comparison of temperature measurement by our sensor and a reference thermocouple

Reference Sensor* Temperature (°C)	Fabricated Sensor Temperature (°C)	Difference (°C)	Reference Sensor* Temperature (°C)	Fabricated Sensor Temperature (°C)	Difference (°C)
21.90	22.42	0.52	799.50	796.97	2.53
22.90	23.15	0.25	799.80	800.25	-0.45
21.70	22.11	0.41	799.20	800.64	-1.44
21.60	22.11	0.51	798.60	795.85	2.75
26.20	26.32	0.12	798.90	796.71	2.19
26.00	26.20	0.20	799.00	802.01	-3.01
23.20	23.22	0.02	800.60	797.77	2.83

^{*}Pt100 is used as reference sensor.

2.8 Discussion

Fiber optic FP temperature sensors have become a widely explored research topic during the last few decades. Most of the sensors use solid material (e.g., glasses, polymers, silicon, etc.) as the sensing element, and have inherent limitations with respect to hightemperature measurement. Many solid materials have a low temperature capability. Their optical properties and sensor structures may also undergo permanent changes at high temperature that lead to sensor signal drift. The uniqueness of the fiber optic temperature sensor studied here is the usage of air as the sensing material and a sensing mechanism that leads to high stability at high temperature. The sensor consists of an FP cavity filled with air whose pressure can be controlled. It utilizes the fact that the difference in air refractive index and unity is proportional to the air pressure and inversely proportional to the air absolute temperature. The optical properties of air are stable at high temperature. The absolute temperature is obtained by measuring the spectra of the FP reflection fringes at two different pressure levels, which is independent of the cavity length. Therefore, even if the enclosure (a glass tube in this case) of the air in the FP cavity were to change its length or undergo permanent deformations at high temperature, it would not affect the accuracy of the sensor.

An assumption we need to make for the sensor to work is that the temperature and the cavity length remain unchanged when the pressure is changed. Therefore, in practical applications, it is critical to ensure that the sensor spectra are measured at two pressure levels within a short time

over which the ambient temperature and the cavity length exert negligible influence. In practical applications, the pressure can reach equilibrium within a few seconds and high-speed spectrometers can be used for spectrum measurement, which means that the temperature and the FP cavity need to be stable over a period of a few seconds.

The use of the gas pressure system increases the size of the sensor system. It also constrains the distance between the sensor head and the pressure devices. In this work, we developed an electronically controlled system with miniaturized and precision devices, making the measurement more practical and ensuring good accuracy and stability. This method can be used in many applications that require a stable and accurate temperature sensor, for example, temperature measurement in coal-gasified power plants.

We also analyzed the contribution of these parameters in temperature measurement deviation. Specifically, we found that the relative wavelength resolution in determining the wavelength shift is the main noise source of the system and its noise contribution is also a function of the temperature itself. This analysis is important for the system design to achieve optimized system performance.

2.9 Conclusion

In this work, we have demonstrated a FP interferometer temperature sensor system based on the spectral shift of fringe wavelength due to the pressure change in FP cavity. Sensor fabrication process is very straightforward, which involved in splicing a fused-silica tube with a regular SMF and a side-hole fiber. Air is passed through the holes of the side-hole fiber to change the cavity pressure up to 100 psi by using a miniaturized pump. The whole pressure calibration and sensor acquisition system is electronically controlled, miniaturized and fast. In addition, we have developed a model to analyze the impact of the system key parameters, such as sensor wavelength resolution and pressure fluctuation on temperature measurement. In the experiment, the sensor has been characterized from room temperature to 800 °C with our setup. The sensor's wavelength resolution is found less than 0.2 pm with a high pressure stability ($\delta P \sim 0.015$ kPa or 2.5×10^{-3} psi). According to our model, this resolution and pressure fluctuation can contribute to a temperature resolution of ± 0.32 °C, which is excellent compared to other fiber optic sensors especially for this broad range of temperature.

The repeatability of the sensor is tested by undergoing it through several thermal cycles from room temperature to $800\,^{\circ}\mathrm{C}$ and comparing it to a high accuracy reference thermometer. The comparison demonstrates high accuracy of the sensor even after multiple cycles.

CHAPTER 3

TEMPERATURE MEASUREMENT USING DUAL AIR-FILLED FABRY-PÉROT CAVITIES WITH VARIABLE PRESSURE

In this chapter, we have presented a modified approach to our previous method of temperature measurement by using two FP cavities placed at differential temperatures. This method neither requires to read pressure nor the knowledge of gas characteristic constant α . Temperature is deduced from the two FP sensor's wavelength shift and the reference FP's temperature, which is known by a trivial sensor. Most of the contents of this chapter are published in **IEEE Photonic Technology Letters** [63] and reproduced here with permission from the publishers – IEEE.

3.1 Introduction

The demand for high-performance fiber optic temperature sensors has witnessed a significant upswing in modern industries, driven by the imperative need for precision and reliability in temperature monitoring. As industries increasingly adopt advanced technologies and processes, there is a growing recognition of the limitations of conventional temperature sensing methods. Fiber optic temperature sensors offer a compelling solution by providing the inherent advantages of optical fibers, such as immunity to electromagnetic interference, minimal signal degradation over long distances, and the ability to function in harsh environments.

The most crucial challenges that the concurrent fiber optic sensors meet are the susceptibility to cross-strain interference, sensor's degradation and shift at elevated temperatures and long-term instability. To overcome these, we have demonstrated a method that uses gas (e.g. air) as the material for the sensing element in the previous chapter [60]. It has a structure of a FP interferometer, whose cavity is filled with gas whose pressure can be controlled and varied. For ideal gases, the difference between gas refractive index and unity (n-1) is linearly proportional to pressure and inversely proportional to absolute temperature with a proportion coefficient α . As the gas pressure varies, the FP fringes shift linearly with pressure. The slope of spectral shift of the FP is proportional to temperature and can be used to deduce temperature using coefficient α . This method eliminates the cross-sensitivity to strain as the strain does not affect the slope of the spectral shift vs. pressure

curve. Many gases have a stable optical property at high temperatures, and using gas as the material for the sensing element renders good long-term stability and no hysteresis. Nevertheless, the accuracy in temperature measurement is largely dependent on the pressure stability and pressure reading accuracy as well as the accuracy in determining coefficient α . In this Chapter, building upon the previous work, we present a new approach for high temperature measurement that requires neither pressure readings (although a trivial low-temperature sensor is needed) nor the information of α , eliminating the need for a bulky pressure transducer and optical characterization of the gas, resulting in simpler and cost-effective instrumentation.

3.2 Principle of Operation

The sensor system, schematically shown in Figure 3.1(a), consists of a pair of FPs filled with gases whose pressure can be varied simultaneously and identically. One of these sensors is placed at high temperature T (to be measured) and the other at ambient known temperature T. The details of the sensor-head are shown in inset, and the notions are explained in the theory section later. The spectral fringes of both FPs shift to the higher wavelength as pressure increases. As shown in Figure 3.1(b), the amount of spectral shift for each FP is related to the temperature of the gas in the FP. As described below, by measuring the fringe shifts of the two FPs, we can deduce the unknown high temperature from the known low temperature without the need to know the pressure.

The wavelength of the fringe valley for an FP, λ , is given by [12],

$$\lambda = \frac{2nl}{m} \tag{3.1}$$

where, n is the refractive index of gas filling the FP cavity, l is the cavity length, and m is the order number of the fringe valley. We used air as the sensing material in the FP cavity. The difference between the refractive index (n) of air and unity is, to a high degree of accuracy, proportional to pressure P and inversely proportional to absolute temperature T [12], or

$$n - 1 = \frac{\alpha P}{T} \tag{3.2}$$

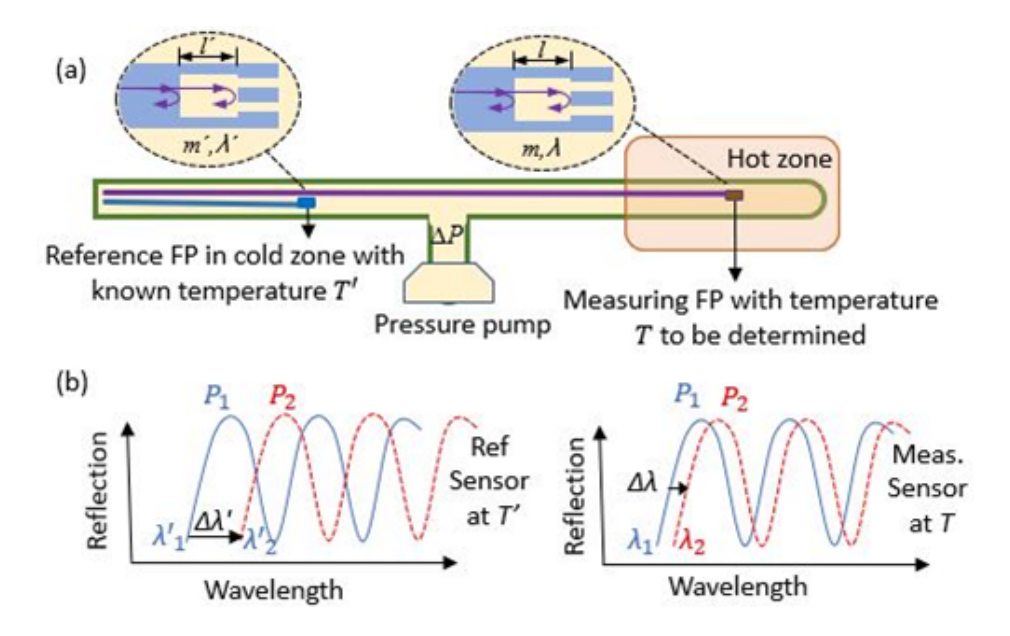


Figure 3.1 Schematics of (a) the sensor system with dual FPs, and (b) spectral shifts with pressure for both FPs.

where α is a constant characteristic of air, which is stable up to a broad temperature range. Combining 3.1 and 3.2 yields,

$$\lambda = \frac{2l}{m} \left(\frac{\alpha}{T} P + 1 \right) \tag{3.3}$$

The pressure P of the cavity can be varied by passing air through the ventilating holes of the sensor. If we change the pressure from P_1 to P_2 ($P_2 \gg P_1$), the corresponding wavelength of the two pressures will be as following:

$$\lambda_1 = \frac{2l}{m} \left(\frac{\alpha}{T} P_1 + 1 \right) \tag{3.4}$$

$$\lambda_2 = \frac{2l}{m} \left(\frac{\alpha}{T} P_2 + 1 \right) \tag{3.5}$$

Subtracting Eq. 3.4 from Eq. 3.5 yields the shift of the wavelength $\Delta \lambda$,

$$\Delta \lambda = \frac{2l}{m} \frac{\alpha}{T} \Delta P \tag{3.6}$$

where $\Delta P = P_2 - P_1$ is the change in pressure. If we consider another FP with a cavity length of l' and mode number m', placed at a known ambient temperature T' and subjected to the same differential pressure ΔP , its spectral shift will be:

$$\Delta \lambda' = \frac{2l'}{m'} \frac{\alpha}{T'} \Delta P \tag{3.7}$$

Dividing Eq. 3.7 by Eq. 3.6 yields,

$$\frac{\Delta \lambda'}{\Delta \lambda} = \frac{l'm}{lm'} \frac{T}{T'} \tag{3.8}$$

Note that for gases, $n \approx 1$ or $\alpha P/T \ll 1$. Applying this approximation in Eq. 3.4 and Eq. 3.5 leads to $l'm/lm' \approx \lambda_1'/\lambda_1$. Then Eq. 3.8 can be written as:

$$T = \frac{\Delta \lambda'}{\Delta \lambda} \frac{\lambda_1}{\lambda'_1} T' \tag{3.9}$$

According to 3.9, with the information of temperature T for the reference FP, we can deduce the high temperature T from the initial wavelength of two FP sensors and their spectral shift with pressure. Thus, this method renders all the benefits of our previous works with a reduced instrumentation since it does not require accurate pressure control and pressure measurement.

3.3 Experiment

The two FPs were fabricated by fusing a silica tube between a single mode fiber (SMF-28, Thorlabs) and a side-hole fiber (TH1088, Fibercore) following the process described in Ref. [13]. The silica tube has an inner diameter of 75 μ m and outer diameter of 150 μ m, slightly larger than the outer diameter of the fiber (125 μ m). Figure 3.2 shows the schematic of the sensor and Figure 3.3(a) and Figure 3.3(b) show the cross-sectional view of the silica tube and side-hole fiber, respectively. The silica tube forms the FP cavity and is filled with air whose pressure can be varied by passing air through the holes of the side-hole fiber (ID: 25 μ m). Figure 3.3(c) and Figure 3.3(d) are the microscope images of the two FPs.

The reflection spectra of the two FPs at ambient temperature and pressure is shown in Figure 3.4. The free-spectral ranges of the two FPs are 10.1 and 12.5 nm, respectively, corresponding to

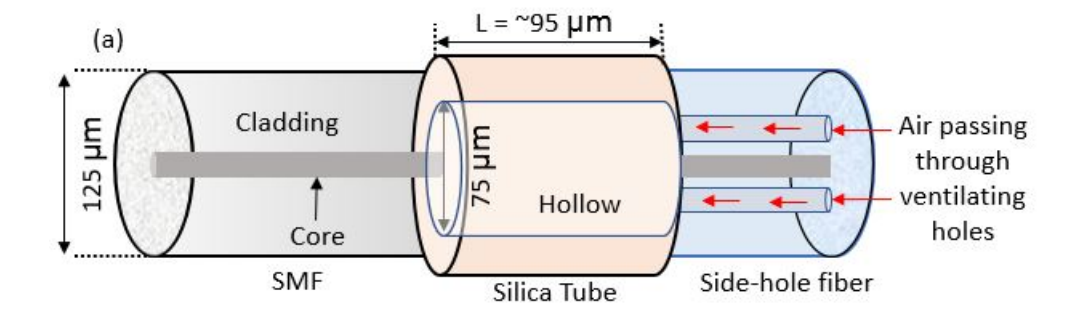


Figure 3.2 Schematic of the sensor.

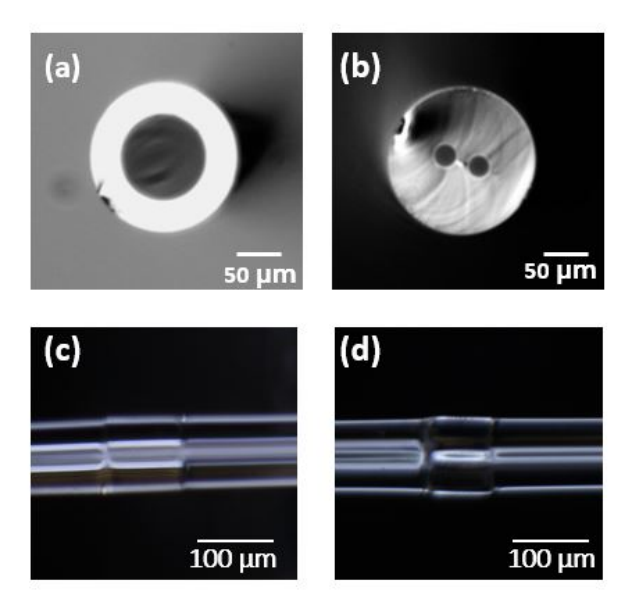


Figure 3.3 Cross sectional view of (a) silica-tube and (b) side-hole fiber, respectively, used in FP sensor fabrication, (c) and (d) microscopic view of the fabricated sensors.

cavity lengths of 119 and 96 μ m, respectively. We opted for the sensor with higher visibility (~ 18 dB) as the measuring FP sensor placed in the hot zone.

To measure the ambient temperature, we used a silicon FP sensor S_{ref} we fabricated previously [14]. It is composed of an 80 μ m long silicon pillar attached to the end of a SMF by UV curable glue. The sensitivity is found experimentally 89.52 pm/°C by a linear fitting. The choice of this sensor is not a necessity but simply for our convenience. Because of the low temperature of the reference FP, many low-cost electronic sensors can be used in practical applications.

Figure 3.5 shows the schematic of the experimental setup for high temperature measurement.

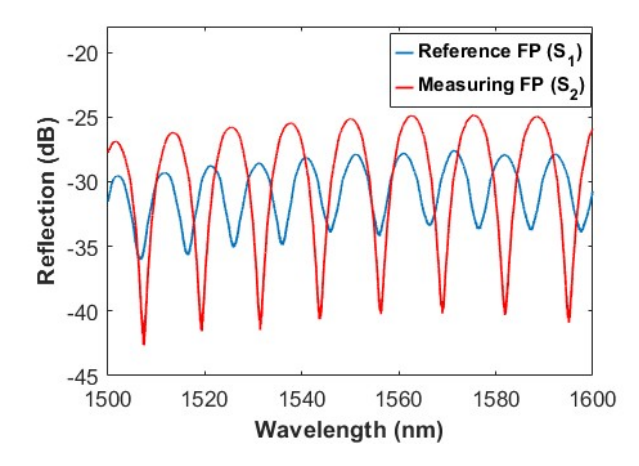


Figure 3.4 Reflection spectra of the sensors at room temperature and room pressure.

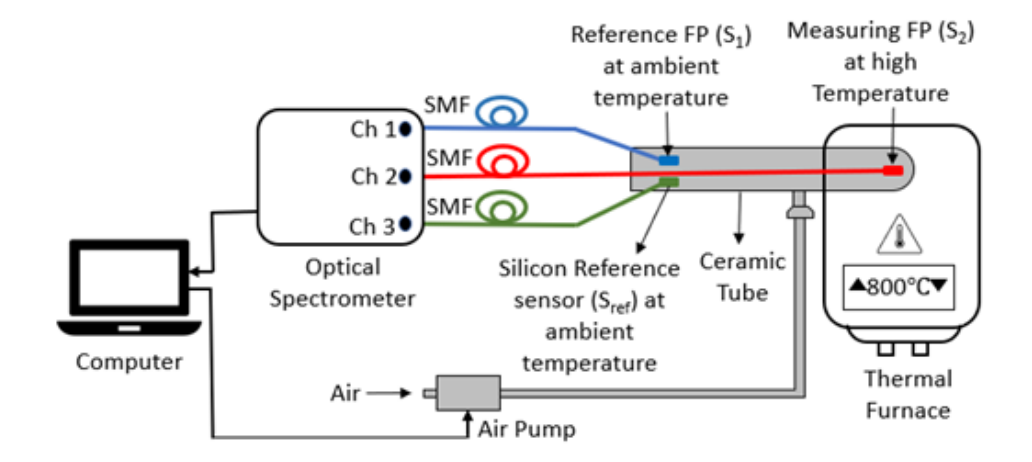


Figure 3.5 Schematic of experimental set up for testing the dual FP sensor system.

The three sensors (two air-filled FP cavities—reference FP S_1 and measuring FP S_2 , and one silicon pillar FP sensor for low temperature measurement, S_{ref}) were connected to different channels of an optical sensor interrogator (Model: Hyperion Si-155, Luna Inc.) for simultaneous acquisition of the reflection spectra of all the sensors. The measuring FP S_2 was placed inside of a thermal furnace and the other two sensors were kept in the cold zone outside of the furnace. All three sensors were housed in a ceramic pipe, whose pressure was controlled by a miniaturized pressure pump and an electric shut-off valve. Although any two pressure levels can be used for spectral shift, we used 0 psi and 90 psi, as P_1 and P_2 , respectively, since it took only few seconds for the pressure to change from P_1 to P_2 and stabilize, which facilitates the real time measurement of temperature. Figure

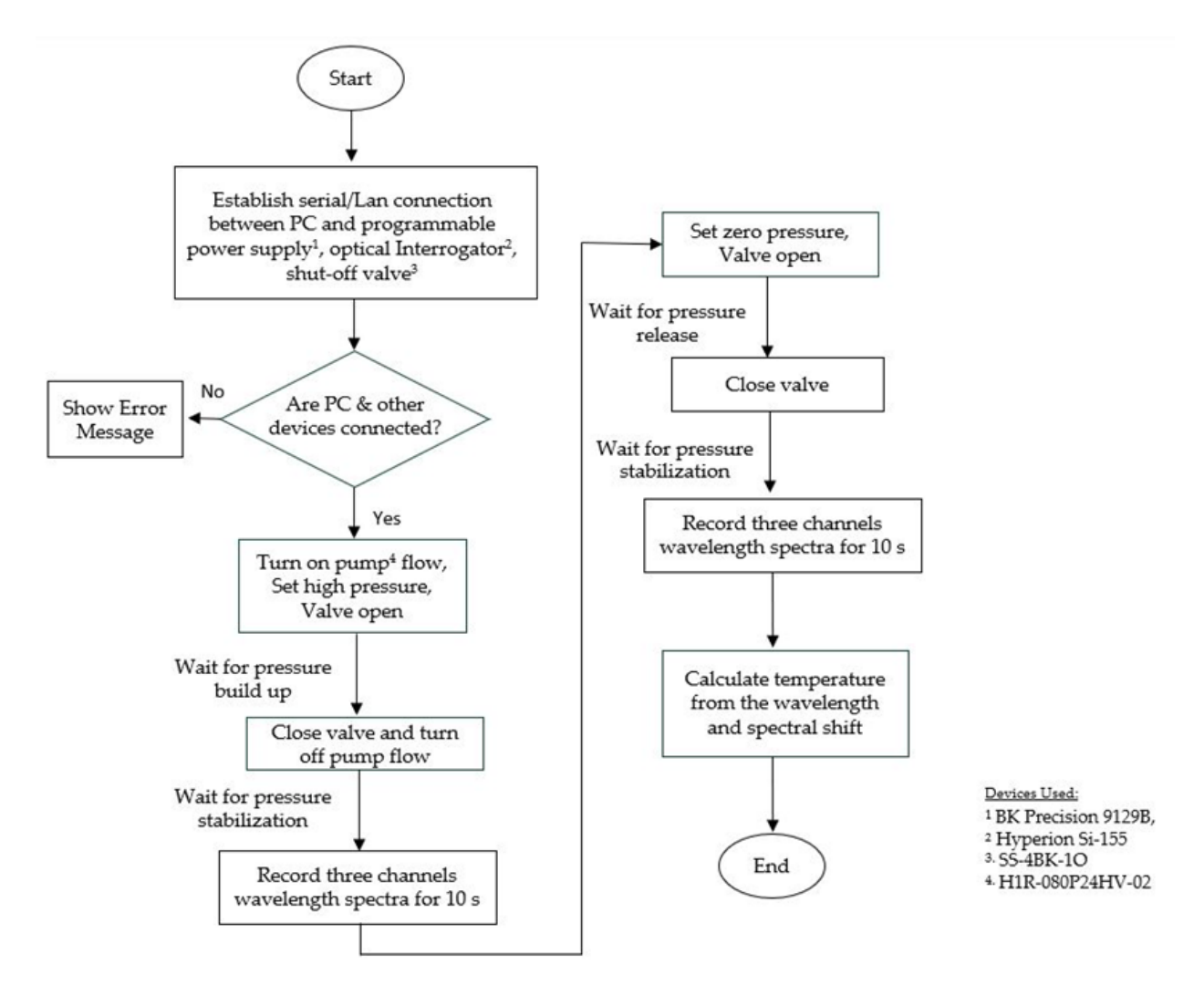


Figure 3.6 Flowchart of the program developed for real-time measurement.

3.6 shows the Matlab program algorithm developed for the real-time temperature measurement. The distance between the thermal furnace and the ambient temperature sensor was kept 30 cm to prevent air conduction through the ceramic pipe to protect the reference sensor.

3.4 Results and Analysis

Using the experimental setup described above, we have tested the dual sensor configuration method as per Eq. 3.9 for a broad temperature range from 25 °C to 800 °C with an increment of 25 °C. For each measurement, we have recorded the reflection spectra in the range of 1500-1600 nm for 10s of duration with a scanning rate of 1 kHz using the interrogator. For each spectral frame, the wavelengths of all fringe valleys were calculated by curve fitting and the average wavelength

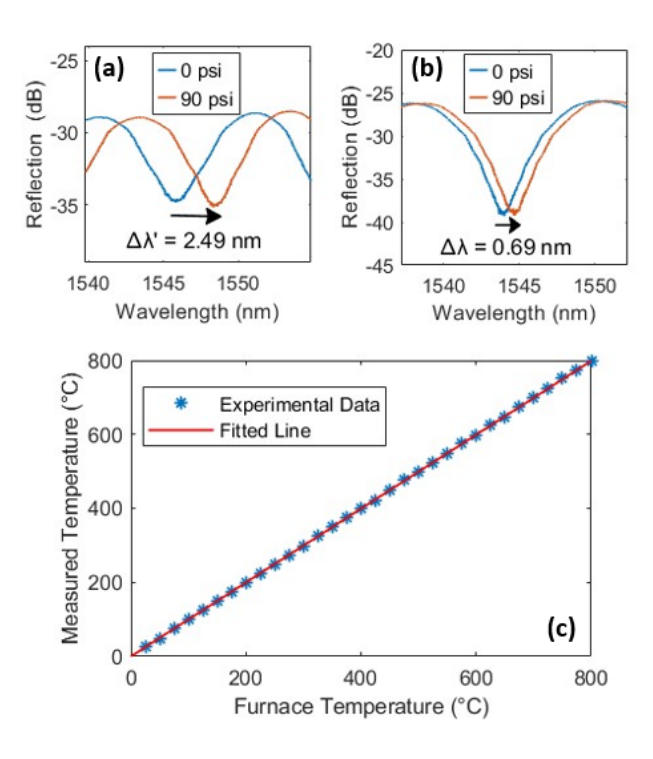


Figure 3.7 (a,b) Reflection spectra of the reference FP at room temperature (a) and measuring FP at $800 \,^{\circ}$ C (b) at two different pressure levels, (c) measured temperature vs set temperature in the furnace.

was used as the fringe wavelength in calculating the wavelength shift in Eq. 3.9. More details on the signal process can be found in [14]. Figure 3.7(a) and (b) shows the spectra of the reference FP at room temperature and the measuring FP at 800 °C when the pressure increased from 0 to 90 psi, highlighting the difference in the spectral shift of the two FPs. Figure 3.7(c) shows the comparison between the measured temperature and the set temperature of the furnace, where the linear fitting line has an R-square of 0.99998, indicating excellent linear response of the sensor system. The measured temperature deviates from the furnace temperature by no more than ±3 °C in each case in this broad temperature range. This slight discrepancy is anticipated since the furnace's accuracy tolerance and temperature uniformity are deteriorated at high temperatures like 800°C.

We studied the measurement resolution of the sensor system by performing the noise analysis for temperature measurement. According to Eq.3.9, the only noise source is the uncertainty in determining the fringe valley wavelengths of the FPs. Because the average wavelengths of the fringe valleys in the range of 1500-1600 nm were used for both FPs in calculating the temperature,

the ratio of average wavelengths of both sensors $\lambda_1/\lambda_1' \approx 1$. Therefore, for the purpose of noise analysis, we modify Eq. 3.9 to

$$T = \frac{\Delta \lambda'}{\Delta \lambda} T' \tag{3.10}$$

Differentiating Eq. 3.10 with respect to $\Delta \lambda'$ and $\Delta \lambda'$ succeedingly, and after some simplifications, we get

$$\frac{\delta T}{T} = \frac{\sqrt{2}\delta\lambda_1'}{\Delta\lambda'} \tag{3.11}$$

$$\frac{\delta T}{T} = \frac{\sqrt{2}\delta\lambda_1}{\Delta\lambda} \tag{3.12}$$

where, $\delta \lambda'_1$ and $\delta \lambda_1$ are the standard deviations of fringe valley wavelength determinations for the reference FP and the measuring FP, respectively. Assuming that obtained fringe valley wavelengths are random independent variables, the total error in temperature measurement can be obtained by taking the sum of the square root of the individual contribution as following,

$$\frac{\delta T}{T} = \sqrt{2} \sqrt{\left(\frac{\delta \lambda_1'}{\Delta \lambda'}\right)^2 + \left(\frac{\delta \lambda_1}{\Delta \lambda}\right)^2}$$
 (3.13)

During the temperature measurement test, the valley wavelengths were recorded for a duration of 10 seconds for each measurement. By taking the standard deviation of the arithmetic average of the valley wavelengths, we obtain the values of $\delta\lambda'_1$ and $\delta\lambda_1$, which represent the resolution of the reference FP and the measuring FP, respectively. Figure 3.8(a) shows the results for both FP sensors at different temperature levels. It is seen that the wavelength noise is less than ± 3 pm for each case and uniform over a broad temperature range from room temperature to 800 °C. Using these experimentally obtained values of spectral shift, $\Delta\lambda'$ and $\Delta\lambda$ at different temperatures, the temperature resolution was calculated using Eq. 3.13 and the results are shown in Figure 3.8(b). Note that, as indicated by Eq. 3.13, the resolution increases proportionally with absolute temperature T. This can also be understood by considering that the spectral shift of the measuring

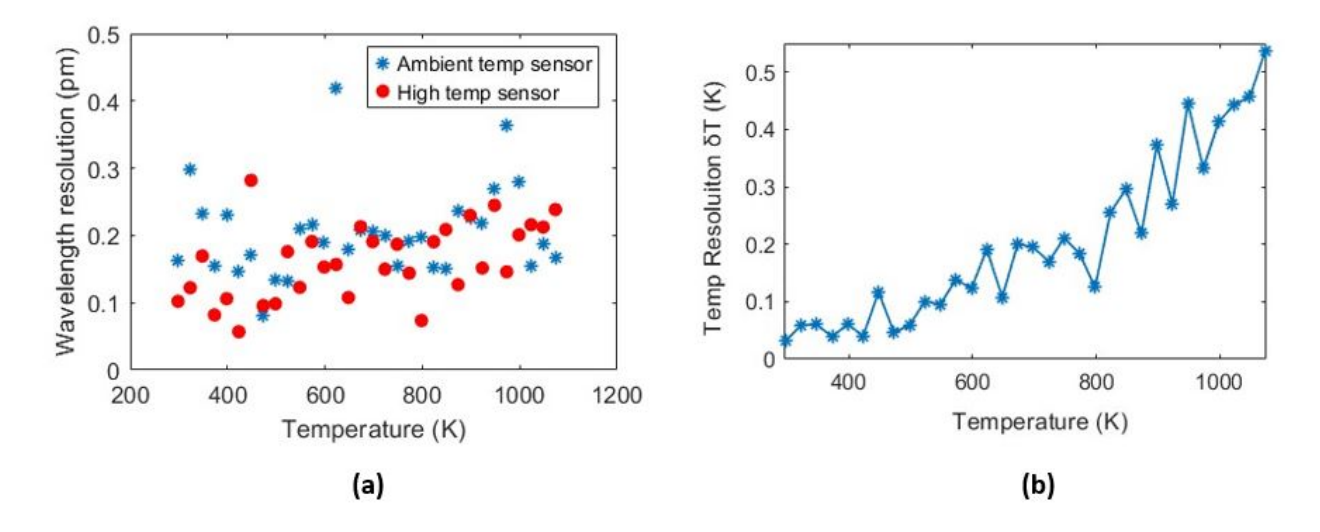


Figure 3.8 (a) Standard deviation (resolution) of fringe valley wavelength determination at different temperatures of the reference FP and the measuring FP, (b) temperature resolution from room temperature to $800\,^{\circ}$ C.

FP, $\Delta\lambda$, is smaller at a higher temperature T for a given pressure change. According to Eq. 3.9, as $\Delta\lambda$ shows up in the denominator, the same level of uncertainty from wavelength determination will lead to a larger uncertainty of T. Nevertheless, the maximum resolution is found to be ± 0.52 °C at 800 °C, which shows high accuracy of the sensor compared to conventional thermocouples and other fiber optic sensors.

We conducted a long-term high temperature test to investigate the stability of the sensor system. The furnace temperature was set at 800 °C (1073 K) and the measuring sensor was kept in the furnace for more than 100 hours. Figure 3.9 shows the measured temperature at different times. The result shows that the mean of the measured temperature is 1072.27 K (799.92 °C) with a standard deviation of ±2.92 K. This deviation in is due to the inaccuracy and non-uniform heat distribution of the furnace used in the setup. Despite these limitations, the fluctuation remains below 0.3% of the absolute temperature, which is an indicator of the accuracy and stability of our proposed method of temperature measurement.

3.5 Discussion

We have demonstrated a modified approach for the fiber-optic temperature sensor method based on air-filled FP cavity with differential pressure. In this approach, we used two sensors at different

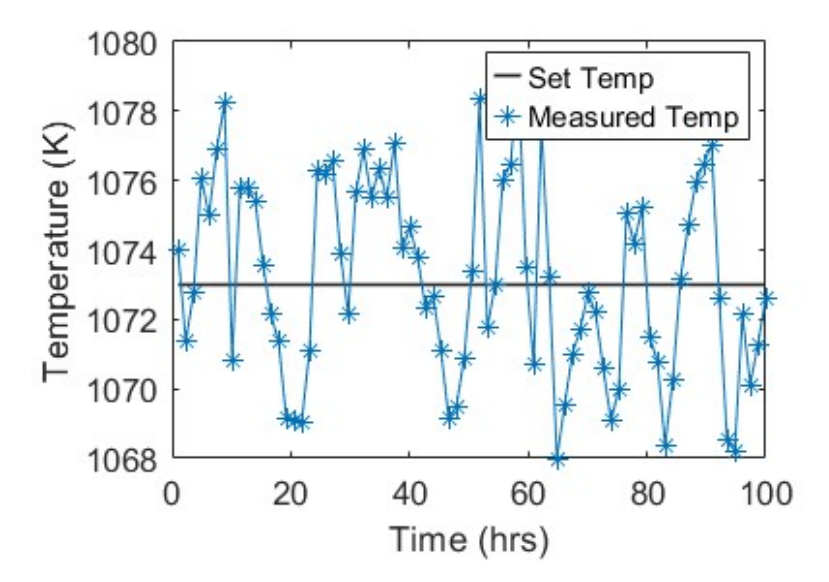


Figure 3.9 Long-term stability test: measured temperature at different times when the furnace was set to $800 \,^{\circ}\text{C}$ (1073 K) for 100 hours.

temperatures- one in an ambient environment and the other at hot area, whose temperature is to be measured. The ambient temperature can be known by using any trivial low temperature sensor (we used a silicon FPI). By combining these two sensors, we can measure the temperature for a broad range (room temperature to 800 °C) with high accuracy. This dual FP cavities approach has some pros and cons compared to our previous method with a single FP sensor and a pressure sensing device. These are described below:

Pros:

- 1. We do not need any pressure sensing device in this method, which makes the instrumentation simpler and relatively cost-effective.
- 2. Data acquisition is easier since a high-speed multi-channel spectrometer can synchronize all the sensors' wavelength data at a faster speed.
- 3. Direct temperature measurement is possible without calculating the slope coefficient S and gas material property α .

4. For the two different pressure levels, we assume that the temperature remains constant. But there was no way to ensure this in the previous method. But in this modified approach, we can measure this temperature with the help of a reference sensor during pressure change to verify if our measurement is consistent with the assumption.

Cons:

- 1. For this method, two air-filled FP cavity sensors are required in addition to an independent reference sensor for ambient temperature measurement.
- 2. The reference FP needs to be isolated from the measurement area and this distance can reduce the spatial resolution.

3.6 Conclusion

In this chapter, We have presented a novel approach to measure high temperature using a measuring FP and a reference FP, with one of them having a known temperature in the cold zone. Both FP cavities are filled with air of identical pressure. The air pressure can be varied, and the temperature of the measuring FP can be deduced by the spectral fringe shift vs. pressure of the two FPs. This method does not require measurement of the pressure or the knowledge of the optical properties of the gas. Experimental results showed that the sensor is capable of measuring temperature up to 800 °C with good linearity. We also studied the noise performance which reveals a high resolution of ± 0.52 °C at 800 °C. Furthermore, a long-term test conducted at 800 °C exhibited the stability of the sensor with fluctuations of $\leq 0.3\%$ over a duration exceeding 100 hours. In the future, we plan to study the spatial resolution of the sensor, which is mostly determined by the thermal spatial profile of the air in the tube at thermal equilibrium. This method can be used in applications where accurate measurement of high temperature is needed such as power plants, aerospace, and metallurgical processes.

CHAPTER 4

SIMULTANEOUS TEMPERATURE AND STRAIN MEASUREMENT BY CASCADED FIBER BRAGG GRATING-SILICON FABRY PÉROT INTERFEROMETER

In our previous chapters, we discussed our novel methods of temperature measurement using air-filled FP cavities. These methods eliminate the effect of cross-strain sensitivity by controlling the pressure in FP cavity. But in many applications, we may need to measure multi-parameters (temperature and strain) simultaneously. In this chapter, we presented a novel sensor based on cascaded fiber-Bragg grating-silicon Fabry-Pérot interferometer to measure temperature and strain simultaneously without cross-interference.

4.1 Introduction

Temperature and strain are two key parameters to monitor for safety purpose, and enhancing the efficiency of many modern industries, including aerospace, petroleum and mining, power plants, structural health monitoring and biomedical applications [64, 65]. But these two parameters are inter-related to each other, and hence it becomes difficult to measure both simultaneously with high accuracy. Conventional thermocouples and strain gauges are used to measure these parameters; however, these have drawbacks of complex wiring, cross sensitivity, long term drift, and signal demodulation limitation [66]. Fiber optic sensors have gained popularity as an alternative to thermocouples and strain gauges due to their many unique advantages, such as small size, high accuracy, immunity to electromagnetic interference, harsh environment compatibility and multiplexing capacity [3].

In the last few decades, many research have been conducted on multiparameter measurement using fiber optic sensors, mostly fiber Bragg grating (FBG) [67, 68, 69], Fabry-Pérot interferometers (FPI) [70, 71], Brillouin frequency shift [12, 13], and fiber loop ringdown [14, 15]. To measure multiple parameters simultaneously, we need at least two characteristic indicators (wavelengths, phase, intensity) with different sensitivities to different measurands (temperature, strain, pressure etc.). Demodulation of the measurand's value is performed by the sensitivity matrix or characteristic equations [72]. However, these methods have some limitations, such as complex fabrication

process, limited sensitivity to prevent temperature cross-talk, multiplexing and interrogating several fibers etc. For example, a typical FBG has temperature and strain sensitivity as 12 pm/°C and 1 $pm/\mu\epsilon$, respectively, which limits its operation in harsh environment with significant fluctuations in strain/temperature. To enhance the sensitivity, researchers have proposed various configurations of the sensor. Tian et al. [69] has proposed a dual FBG configuration incorporated with capillary tube, where the strain and temperature sensitivity were increased to 5.46 pm/ $\mu\epsilon$ and 15.7 pm/°C, respectively. Ref [67] used a single FBG, partly bonded and partly unbonded to the host structure to discriminate strain and temperature sensitivity, but the low sensitivity issue of FBG to strain remained unanswered. In recent time, a new scheme is invented where two FPI sensors are used to form optical vernier effect [73, 74, 75] for enhanced sensitivity. Although this configuration renders well for single parameter measurement, it needs an isolation technique between the reference FP and measuring FP to minimize cross-talk for simultaneous measurement. Hence it is not practical in many applications. Another prospective research on strain sensor characterization is to analyze the strain induced by the thermal expansion of the host structure to which it is attached. This becomes more significant at elevated temperatures and causes error in measurement. Many of the abovementioned works did not characterize their sensor's performance attaching it to a structure to monitor thermal strain.

In this work, we introduced a novel configuration of a FBG-FPI sensor to simultaneously measure temperature and strain with significantly improved temperature sensitivity and reduced cross-talk. The sensor is composed of a FBG inscribed in a single mode fiber (SMF) and a 100 μ m long silicon tip attached to its end to form a FP cavity. This silicon tip FPI is free from strain sensitivity because it is not bonded to the host structure. Again, the high thermo-optic and thermal expansion coefficients of silicon compared to silica-based fiber results in six times improved temperature sensitivity (89 pm/°C). This facilitates the high-accuracy temperature measurement free from cross-strain interference. On the other hand, the FBG wavelength will be shifted due to both temperature and strain changes in the surroundings. In this paper, we characterized the FBG with varying temperature without any load and varying load without changing temperature

to obtain its thermal and mechanical strain sensitivity, respectively. Using these values, we can demodulate the temperature, thermal strain, and mechanical strain data from the cascaded FBG-Si FPI sensor spectrum for multiparameter measurement. The high sensitivity, enhanced resolution, and small size of the sensor can render practical applications where accurate measurement of strain and temperature is required.

4.2 Sensor Fabrication

Our proposed sensor consists of a FBG inscribed in a SMF and a silicon pillar attached to the edge of this to form FP cavity. Figure 4.1 shows a schematic of the sensor. For fabrication, we first wrote a FBG of 5 mm length and Bragg wavelength of 1549.5 nm on a coating-removed single-mode fiber following standard phase mask technology. Excimer laser (193 nm) was irradiated with 5 mJ pulse energy and 500 Hz frequency for 1 minute to write gratings through a cylindrical lens and a phase mask (pitch 1072.0 nm). Figure 4.2 shows the schematic of the FBG fabrication process. The initial reflectivity of the FBG was 92%. After fabricating the FBG, we cleaved the edge of the FBG and attached a silicon pillar to the flat end by using UV curable glue. The length of the silicon pillar is 100 µm and diameter is 150 µm. The separation between the FBG and the silicon pillar is optional, depending on the size of the structure to whom it is attached. Theoretically, the strain distribution over the attached FBG will be Gaussian profile, which means the FBG will feel the maximum strain at its center if the whole FBG length is attached to the test structure (shown in Figure 4.3). The fabrication process of the silicon FP is described detailed in [62]. This silicon pillar forms the cavity of the FP interferometer, which will be used for temperature measurement, whereas the FBG will be attached to the test specimen to measure strain.

Figure 4.4 shows the reflection spectrum of the sensor at room temperature measured by an optical interrogator (Luna Hyperion Si-155), which reveals a good visibility of both the FBG peak and FP interferometric fringes. The visibility is optimized such that the FBG peak optical power is in the order of at least two times higher than the FP fringes peak intensity. This helps in signal processing to separate the FBG wavelength from the FP fringes. The free spectral range of the FP valleys is 3.3 nm, which corresponds to a cavity length of \sim 105 μ m, consistent with the silicon

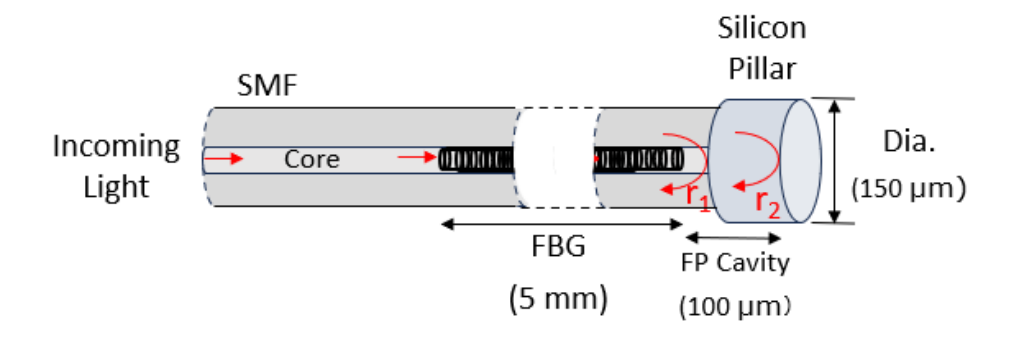


Figure 4.1 Sensor schematic diagram (dimensions are not proportionately scaled).

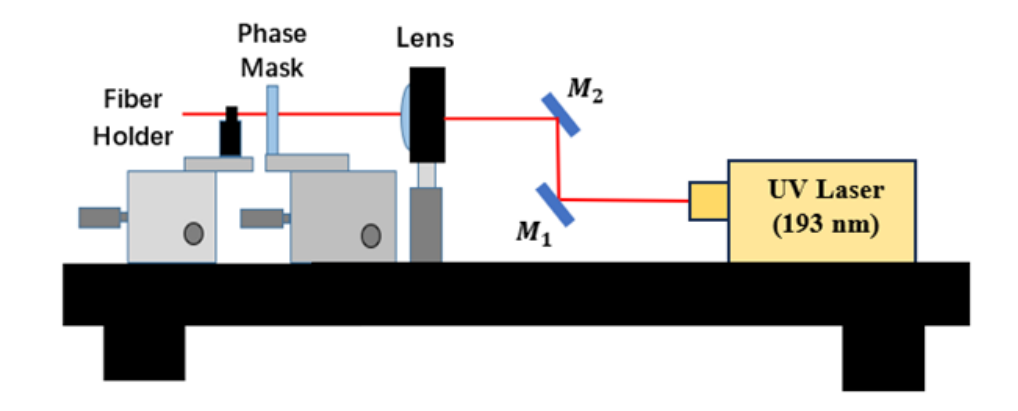


Figure 4.2 Fabrication method of FBG by Excimer laser.

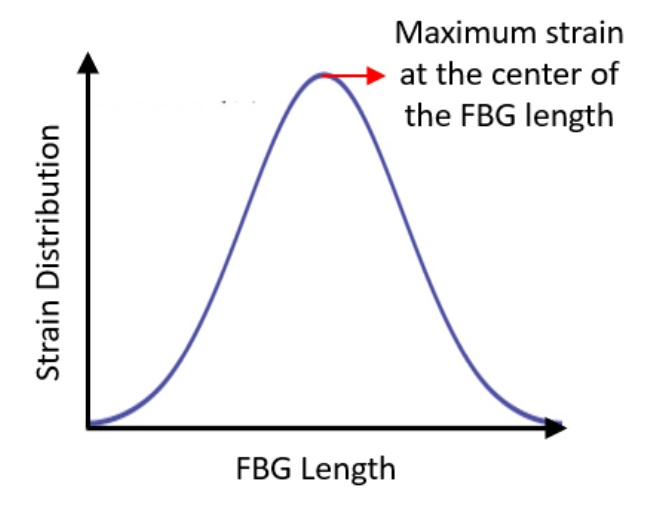


Figure 4.3 Strain distribution profile over FBG length.

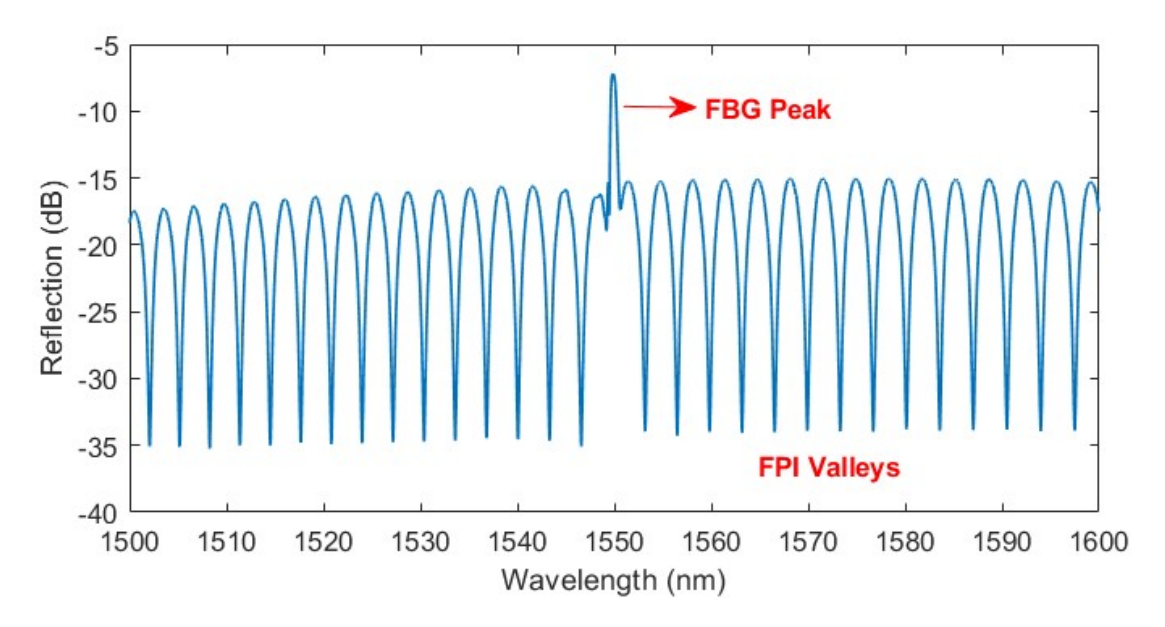


Figure 4.4 Reflection spectrum of the FBG-FPI sensor at room temperature.

pillar length.

4.3 Principle of Operation

The periodic wavelength λ of a FP interferometer fringe valley is as follows,

$$\lambda_{FP} = \frac{2nL}{m} \tag{4.1}$$

where n is the refractive index, L is the cavity length, and m is mode number. On the other hand, the Bragg wavelength of a FBG is defined as,

$$\lambda_B = 2n\Lambda \tag{4.2}$$

where n is the refractive index and Λ is the grating period. In both equations, the refractive index n and characteristic length (cavity length L or grating period Λ) are dependent on the surrounding perturbations, such as temperature, strain, pressure etc. and the sensitivity is dependent on the respective materials. Hence, we can simultaneously measure two different parameters if we can incorporate two different characteristic wavelengths in a single sensor structure with different sensitivities to the measurand variables. This is the main working principle for this research work,

where we measure temperature and strain by monitoring two different characteristic wavelength shifts- valley wavelengths of FPI to measure temperature and Bragg wavelength of FBG for strain measurement.

4.3.1 Temperature Measurement

The temperature effect on the characteristic wavelength can be described as,

$$\frac{d\lambda_n}{dT} = \lambda_n \left(\frac{1}{n} \frac{dn}{dT} + \frac{1}{L} \frac{dL}{dT} \right) \tag{4.3}$$

The two terms inside the parenthesis are known as Thermo-optic coefficient (TOC) and thermal expansion coefficient (TEC), which are 1.5×10^{-4} RIU/°C and 2.55×10^{-6} m/(m·°C) for silicon at room temperature, much higher than silica whose TOC and TEC are 1.28×10^{-5} RIU/°C and 5.5×10^{-7} m/(m·°C) at room temperature [62]. Assuming the refractive index of silicon and silica as 3.4 and 1.445 respectively, the temperature sensitivity according to Eq. 4.3 is found 72 pm/°C for silicon FPI and 14 pm/°C for silica FBG. To take advantage of high temperature sensitivity of silicon, we will use the silicon FP sensor to measure the temperature only, and the FBG will be attached to the test materials whose strain is to be measured. So experimentally the measured temperature will be as follows:

$$\Delta \lambda_{FP} = k_{FP_T} \Delta T \tag{4.4}$$

where, $\Delta \lambda_{FP}$ is the shift of average valley wavelength of the FPI sensor due to the change in temperature ΔT and k_{FP_T} is the temperature sensitivity of the FPI, whose value will be determined by a temperature calibration test in the later section. The comparison between silica and silicon's parameters is shown in Table 4.1.

4.3.2 Strain Measurement without Heat

The Bragg wavelength shift, $\Delta \lambda_B$ due to change in mechanical strain $\Delta \varepsilon_M$ is given by,

$$\Delta \lambda_B = \lambda_B (1 - p_e) \Delta \lambda_M \tag{4.5}$$

Table 4.1 Comparison of silica and silicon materials

Parameters	Silica	Silicon
Thermal Expansion Coefficient (m/(m·°C)	5.5×10^{-7}	2.55×10^{-6}
Thermo-Optic Coefficient (RIU/°C)	1.28×10^{-5}	1.5×10^{-4}
Refractive Index (RIU)	1.445	3.4
Temperature Sensitivity (pm/°C)	14	72

where p_e is the effective strain optic constant and is given by,

$$p_e = \frac{n_{eff}^2}{2} (p_{12} - \sigma(p_{11} + p_{12})) \tag{4.6}$$

where p_{11} , p_{12} are Pockel's constant and σ is Poisson's ratio. For silica made fiber, the value of p_{11} , p_{12} and σ are 0.113, 0.252, and 0.16, respectively [67]. Using these values, we can theoretically calculate the strain sensitivity of a silica-made FBG as 1.2 pm/ $\mu\epsilon$. Experimentally, we can obtain the applied strain by the following formula,

$$\Delta \lambda_{B\varepsilon_M} = k_{\varepsilon_M} \Delta \varepsilon_M \tag{4.7}$$

where $\Delta \lambda_{B\varepsilon_M}$ is the shift in Bragg wavelength of the FBG due to change in strain $\Delta \varepsilon_M$.

4.3.3 Strain Measurement with Heat

For an application, where both heat and strain coexist, the FBG wavelength will shift due to both thermal strain and mechanical strain. This additional thermal strain is due to the thermal expansion of the host material to which the strain sensor is attached. For this case, the total shift in FBG wavelength will be,

$$\Delta \lambda_B = \Delta \lambda_{B\varepsilon_T} + \Delta \lambda_{B\varepsilon_M} \tag{4.8}$$

where $\Delta \lambda_{B\varepsilon_T}$ is the shift due to thermal strain, which is measured from the thermal strain sensitivity of FBG and measured temperature from the FPI sensor.

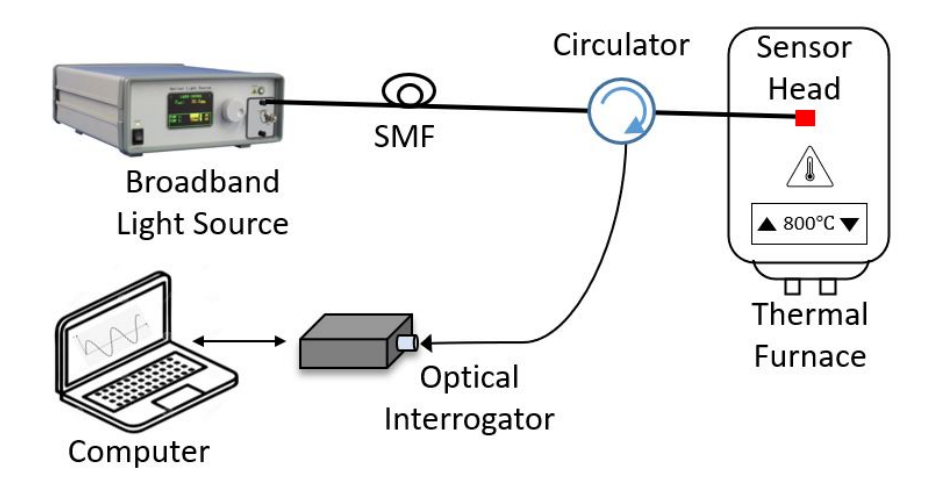


Figure 4.5 Experimental setup for temperature test.

4.4 Experiments and Results

Figure 4.5 shows the experimental setup to test the temperature sensitivity of our fabricated sensor. The sensor is placed inside of a thermal furnace and the temperature was increased from room temperature to 100 °C with an increment of 10 °C. For each temperature reading, we measured the reflection spectrum of the sensor by an optical interrogator with 1 KHz scanning rate for 10 s.

For signal demodulation, we find the wavelength by Gaussian Curve fitting and taking average of multiple valleys of the FPI (details can be found in ref [62]). Figure 4.6 shows the reflection spectra at different temperature. To get a better understanding of the spectral shift, we have drawn two red arrows indicating the shift of the left most and right most valleys with temperature increase. During signal processing, only the valleys within these two arrows were considered for taking average wavelength value. Since the FBG peak is also shifting, the valleys which are affected by the FBG peak (in the range of 1545-1555 nm, shown by a grey area) are filtered out while measuring the average FP wavelength to avoid error.

Figure 4.7(a) shows the shift of the average valley wavelength with temperature. By linear fitting, we found the temperature sensitivity of the FPI is 89.2 pm/°C, similar to the theoretical value. The linear fitting also has a high R-square value (0.9976) which shows excellent linearity of our sensor in this temperature range. Figure 4.7(b) shows the wavelength resolution of the FPI wavelength as 0.17 pm at room temperature. Hence the temperature resolution of our fabricated sensor is found

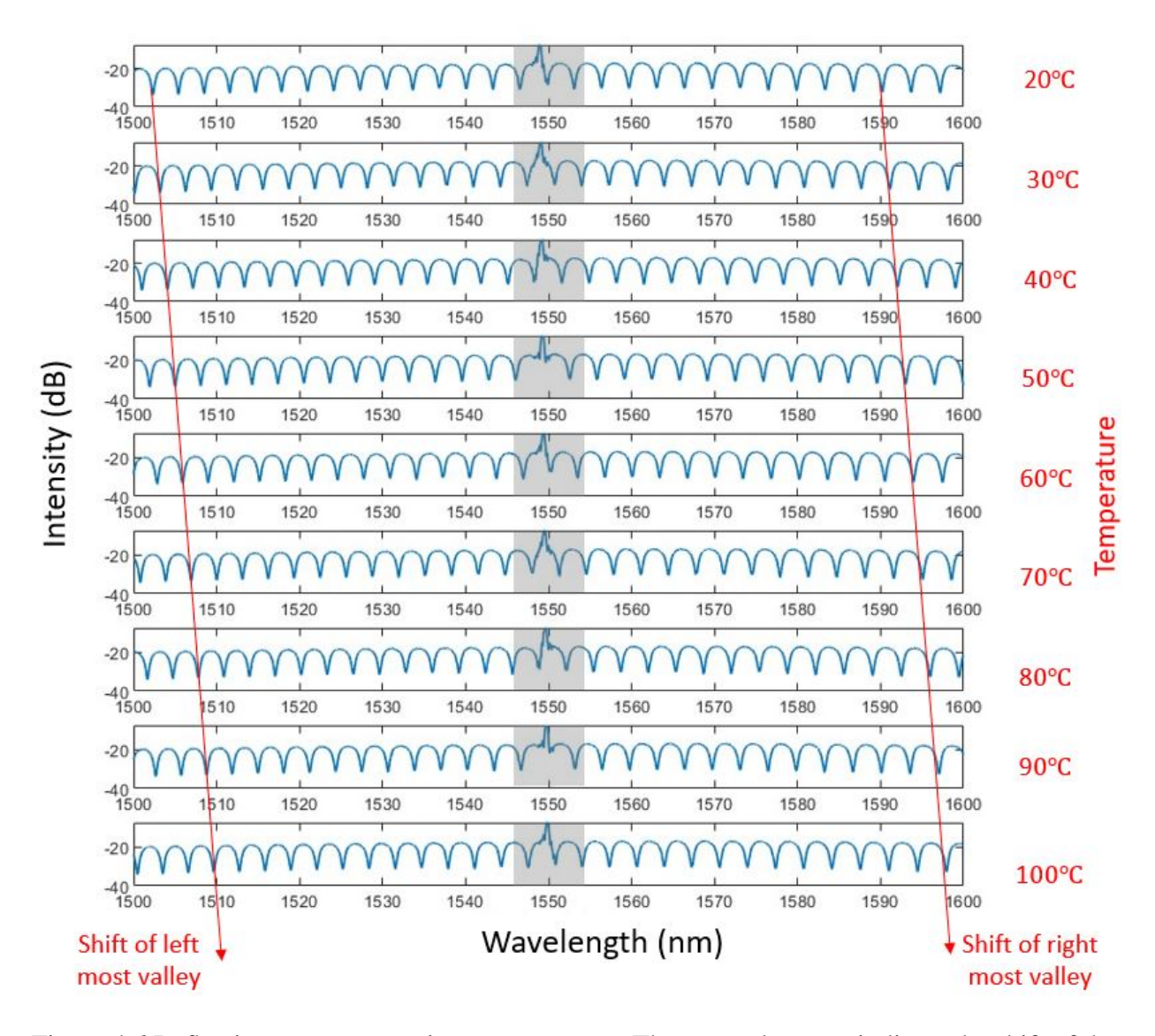


Figure 4.6 Reflection spectra at various temperature. The two red arrows indicate the shift of the left most and right most valley. Grey shaded valleys are affected by FBG shift, hence are filtered out for average wavelength measurement.

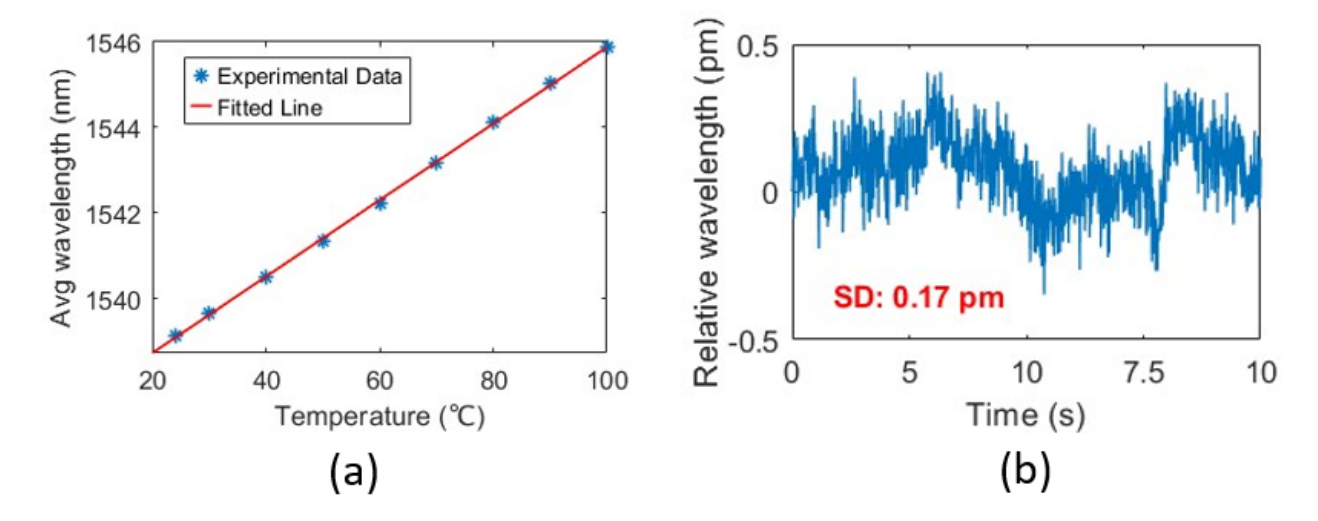


Figure 4.7 (a) Wavelength shift of the FP valleys with temperature, (b) wavelength resolution measured over 10s.

experimentally 0.0019 °C, which is excellent compared to conventional thermocouple or silica based fiber optic sensor.

To measure the strain sensitivity, we attached the sensor to an Aluminum beam of dimension $10 \text{ cm} \times 2.5 \text{ cm} \times 0.47 \text{ cm}$ by using adhesive (Epoxy MS-907). The test specimen was placed in a cantilever setup, where one end of the beam was fixed to a firm support, and the other end was hanging freely where the load (weight) will be applied. Figure 4.8 shows the schematic of the setup for strain measurement.

From the mechanics of materials [76], it is well known that the moment of bending M(x) for a applied load P for such a cantilever setup is given by,

$$M(x) = -Px \tag{4.9}$$

$$or, EI\frac{d^2y}{dx^2} = -Px$$

From the definition of strain ε ,

$$\varepsilon = -d\frac{d^2y}{dx^2} \tag{4.10}$$

where d is the distance from neutral axis to a point along the beam x axis, which is the half of the thickness of the beam in our case.

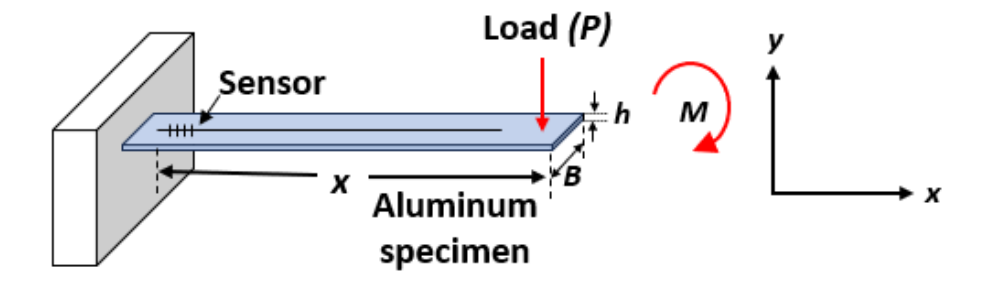


Figure 4.8 Experimental (cantilever) setup for strain measurement.

Combining Eq. 4.9 and Eq. 4.10, the applied strain due to the load in our cantilever setup is as follows,

$$\varepsilon = \frac{Pxh}{2EI} \tag{4.11}$$

where, x is the length from the strain sensor to load, h is the thickness of the specimen, E is the Young's Modulus of Al (69 GPa), and I is the moment of inertia (for a rectangular beam, $I = bh^3/12$, where b and h are width and thickness).

To measure the strain sensitivity of the FBG, we increased load from 0 to 1kg with a step of 100g (equivalent to 14.7 $\mu\epsilon$ strain) on the free hanging end of the aluminum beam in a constant temperature (room temperature, 22 °C). Figure 4.9(a) shows the shift of the FBG peak wavelength with increasing strain. From the linear fitting, the strain sensitivity is found 1.09 pm/ $\mu\epsilon$, which is consistent with the theoretical value. Also, the fitting line has an excellent R-square value of 0.9998, showing good linearity of the sensor. Wavelength resolution of the FBG, obtained by taking the standard deviation of each spectral frame peak wavelength for 10s measured with high-speed I-mon spectrometer (1 KHz scanning rate) is shown in Figure 4.9(b), which is 0.046 pm. Hence, the strain resolution of our fabricated sensor is $\pm 0.042 \mu\epsilon$.

Note that the strain measurement in the previous experiment was performed at a fixed temperature, so the FBG spectral shift was free from cross-temperature sensitivity. But if the test specimen is exposed to elevated temperature, the FBG will be subjected to both thermal and mechanical

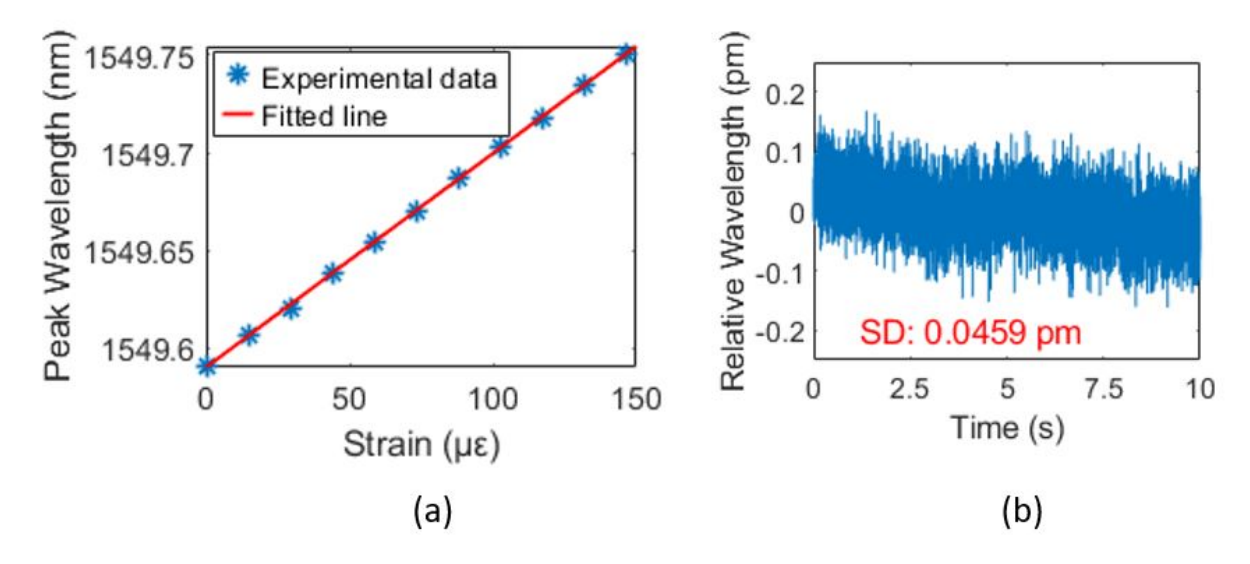


Figure 4.9 (a) Wavelength shift of the FBG peak with strain, (b) wavelength resolution of the FBG peak at initial condition.

strain. This will cause error in strain measurement if the thermally induced strain is not taken into account. To measure the thermal strain sensitivity of the FBG sensor, we placed the sensor inside the thermal furnace and increased the temperature (no load was applied). We compared the FBG shift with temperature for both cases- (i) when it is unbonded (free) and (ii) when it is attached to the aluminum specimen. Figure 4.10 shows this comparison, which reveals that the attached FBG has a spectral shift of 31.36 pm/°C, while the free FBG has a shift of 11.37 pm/°C. The additional shift of the FBG is due to the thermally induced strain of the aluminum specimen. Theoretically, if we put the thermal expansion coefficient of Aluminum $(23 \times 10^{-6} \text{ m/m-K})$ in Eq. 4.3, we find the thermal strain sensitivity of the sensor as 45 pm/°C. In practice, thermal strain is not fully transferred from the aluminum to the FBG due to the inefficient bonding of adhesive and other factors [77]. Still both the slopes in Figure 4.10 have good linearity showing a constant thermal strain transfer of the sensor at different temperatures.

Finally, we conducted an experiment where both temperature and strain were simultaneously varied to demonstrate how to measure these two parameters without cross-sensitivity. For this, we put the cantilever setup (previously used for mechanical strain measurement) inside of a thermal chamber (CSZ Environmental Test Chamber), whose temperature can be varied while we put

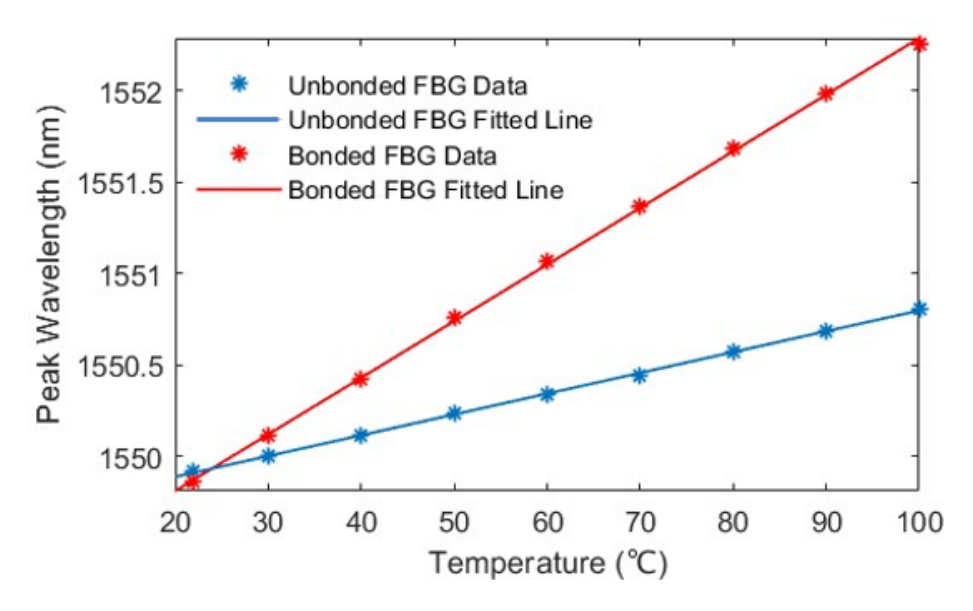


Figure 4.10 Comparison of FBG peak wavelength shift with temperature for unbonded and bonded sensor.

different loads on the test specimen. We measured the sensor spectrum while increasing the temperature from 30 °C to 90 °C with 10 °C increment for four different loads - 0, 250, 500 and 1000 gm (equivalent to 0, 36.65, 73.29 and 146.59 $\mu\epsilon$, respectively). Figure 4.11(a) and (b) show the shift of the FPI and FBG for all cases, respectively. It is seen that the FPI wavelength shift rate is almost the same (89 pm/°C) regardless of whether any strain is applied or not. This indicates that the FPI is free from strain sensitivity. On the other hand, the FBG peak wavelength shifts with a slope close to 1.10 pm/ $\mu\epsilon$, but the data for different loads have offsets due to the additional applied strain. For example, the inset of the Figure 4.11(b) shows that at 80 °C, FBG peak wavelength increases 144 pm from no load to a load of 146.59 $\mu\epsilon$. So, for simultaneous measurement, we first need to obtain the temperature data from the FPI shift, followed by measuring the strain from the FBG shift at that specific temperature.

Here, we need to mention that the strain sensitivity of the FBG is not constant over a broad temperature range. We used a constant value for aluminum's Young's modulus (69 GPa) when calibrating the strain sensitivity in Eq. 4.11. But in practice, Young's modulus for any materials changes with temperature. Especially at an elevated temperature, the reduced value of Young's modulus needs to be considered for accurate strain measurement. Also, the epoxy strain transfer

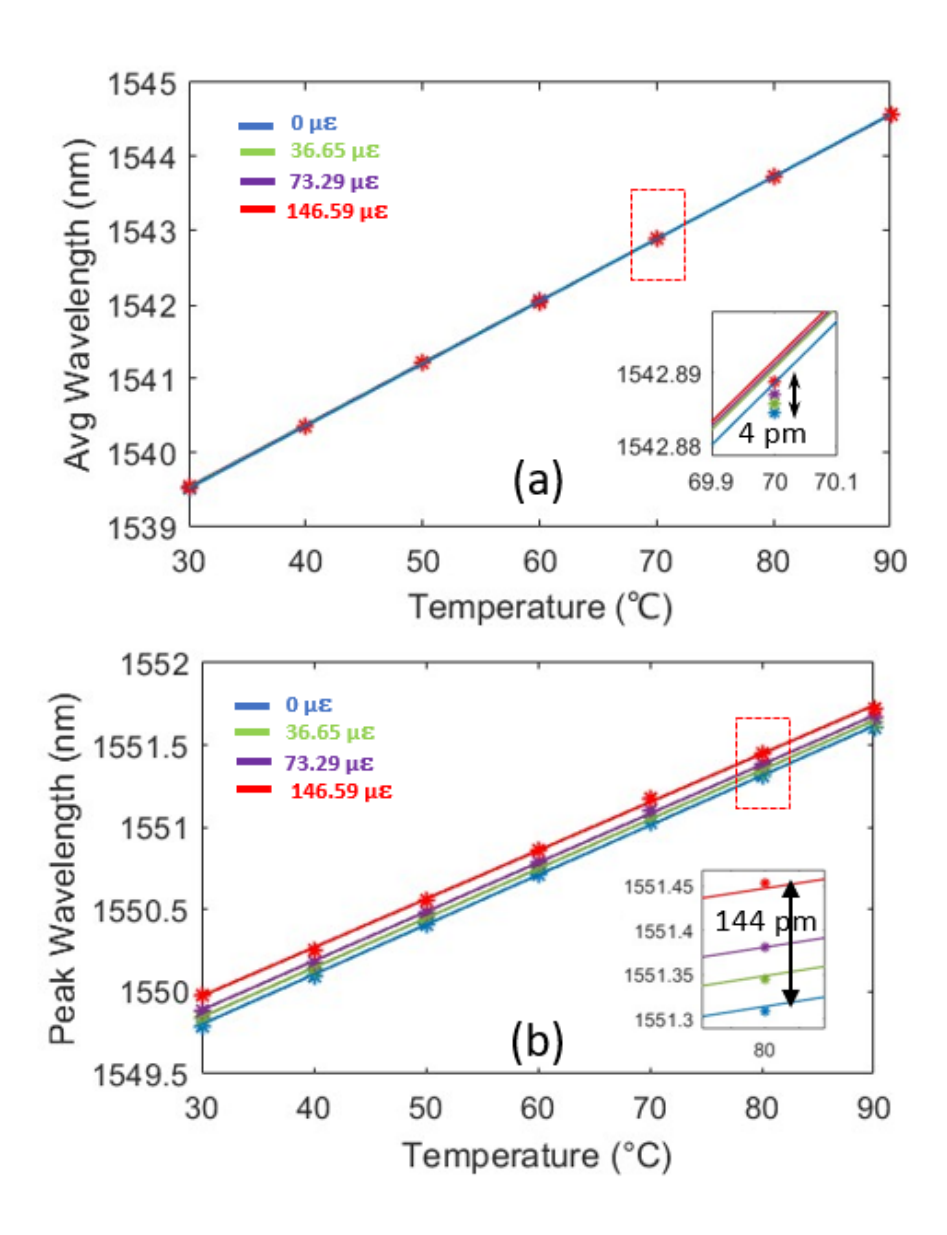


Figure 4.11 (a) FPI and (b) FBG wavelength shift with varying temperature and strain (insets show the zoomed-in view of a specific temperature data).

can be different at higher temperatures, which needs to be calibrated as well.

4.5 Conclusion

In this work, we presented a novel configuration of cascaded FBG-silicon FPI sensor to measure temperature and strain simultaneously. The high thermal expansion coefficient and thermo-optic coefficient of silicon results in the high temperature sensitivity compared to traditional silica based sensor. Also, the work analyzes the shift of the FBG due to the thermal expansion of the host

material to which it is attached to. The experimental results show that this sensor has high temperature resolution of $\pm 1.9 \times 10^{-3}$ °C for the FPI and high strain resolution of $\pm 0.042~\mu\epsilon$ for the FBG, measured by a high-speed spectrometer. The enhanced temperature sensitivity, small size and high resolution can render in many practical applications such as aerospace, civil engineering, and manufacturing industries, where simultaneous monitoring of temperature and strain is crucial for ensuring safety, reliability, and optimal performance of materials and structures.

CHAPTER 5

CONCLUSION AND FUTURE WORK

Our research in this dissertation can be broadly classified into two sections—(i) temperature measurement using air-filled FP cavity and (ii) simultaneous temperature and strain measurement by a cascaded FBG-silicon FPI sensor. In this chapter, we have discussed the concluding remarks, limitations and possible future directions of these works.

5.1 Temperature measurement using air-filled FP cavity

5.1.1 Summary

Fabry–Pérot (FP) interferometers have been widely explored in fiber optic research for the last few decades. The crucial limitations that most of the works have encountered are inaccuracy at high temperature, complexity in the fabrication process, and the susceptibility to cross-sensitivity by strain or pressure perturbations. In this work, we have demonstrated a fiber optic temperature sensor system based on air-filled FP cavity with variable pressure in order to overcome these limitations.

The sensor is fabricated by sequentially splicing a single-mode fiber, a silica tube, and a side-hole fiber. This fabrication method is quite straightforward compared to the sensors that are fabricated by micromachining, complex chemical processes, or expensive high-power laser ablation. With commercially available standard splicing technology, our sensors can be manufactured faster, are highly reproducible, and do not require costly lasers or precision translation motor technology. The most unique advantage of this work is the use of air as its sensing material. Most of the traditional FP sensors are made of graphene, polymer, or other solid material. These materials refractive indices and thermal expansion vary at elevated temperature by a significant factor. Hence the sensors' spectral shift is not linear and becomes complex function of many variables, especially when the temperature is elevated. Researchers often require calibration to measure temperature accurately with these sensors. However, our developed method uses air as its sensing material, which has a very stable refractive index over a long range of temperature (even at 1500 °C). As a result, the sensor exhibits linear characteristics over this broad range. Another unique characteristic

of our proposed method is the fact that the temperature is not derived from the absolute cavity length of the FP sensor. It is obtained by varying pressure and monitoring the corresponding wavelength. So, the temperature is not a function of the cavity length unlike traditional FP sensor. Any change in the cavity length due to the surrounding perturbations (pressure/strain) will not affect the measurement. This working principle effectively eliminates one of the biggest challenges of concurrent fiber optic sensors—susceptibility to cross-sensitivity. It also makes the sensor operation free from any external calibration requirements.

Apart from the theory, we also developed a practical setup for the sensor's operation with miniaturized and electronic-controlled equipment. We wrote a MATLAB program to control the pump, pressure transducer and optical interrogator. This facilitates the measurement system to be real-time, and sustainable for long-term dynamic operation. We verified that even with a small pressure change (like 90 psi or less), the sensor's performance is accurate. Our setup ensures sufficient stability in pressure (<0.2 psi) and wavelength resolution (0.3 pm), which results in excellent temperature resolution (less than 0.5 °C at high temperature of 800 °C). Our theoretical analysis on system parameters (such as pressure and wavelength fluctuations) will help for further system design and accuracy.

For signal demodulation from the optical spectrometer, we used an average wavelength tracking method. Since the FP sensors have many periodic notches in the range of 1500-1600 nm, taking multiple valleys for average helps to reduce wavelength noise significantly. It also removes the complexity and limitations of other signal processing methods (like Fast Fourier Transform in frequency domain).

To verify our proposed method and sensor's performance, we performed three standard characterization test—linearity test (from room temperature to 800 °C), thermal cycle or repeatability test (several heating and cooling from room temperature to 800 °C) and long-term stability test (subjecting the sensor at 800 °C for more than 100 hours). The sensor performed exceptionally well in all cases. The wavelength shift of the sensor has been very linear up to this broad range of temperature and the measured temperature did not deviate from the furnace set-temperature by

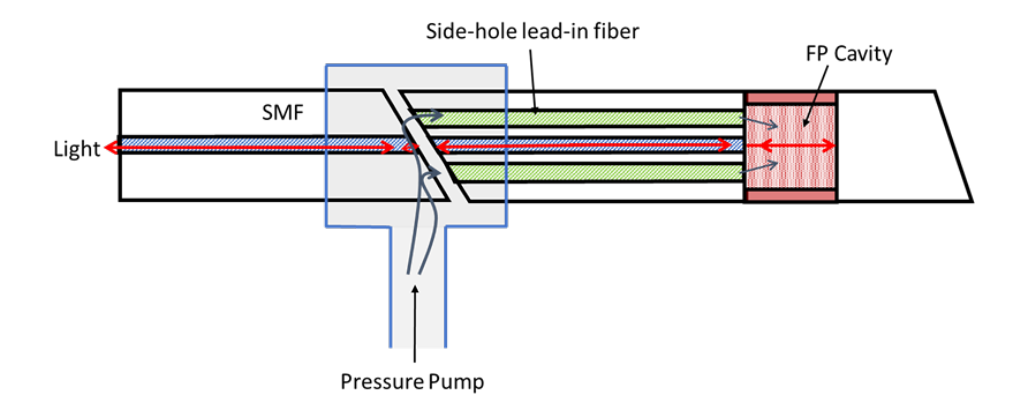


Figure 5.1 Modified configuration with side-hole fiber as lead-in fiber.

no more than ±3°C. Even the sensor provided very accurate measurement when it was subjected to elevated temperature for extended period (more than 100 hours). Hence this method can be used in various applications, where temperature measurement with high-accuracy and long-term sustainability is required.

5.1.2 Future Works

There are many possible future directions in which this work can be explored further. Some of these are discussed as following:

1. Using the side-hole fiber as lead-in fiber for faster pressurization:

Even though we used a very small pressure change to measure temperature, the time required to reach pressure equilibrium still depends on the ceramic pipe size that houses the sensors. This large pipe and the time required for pressure stability can be a limitation to many applications. However, for the sensors presented in our research, it is possible to use side-hole fibers as the lead-in fiber and use the holes in the lead-in fiber to pressurize the FP cavity, as shown in Figure 5.1.

With this configuration, a small 3D-modeled structure can be used to pressurize the cavity through side-holes. This will make the system and sensing element significantly more compact than our current setup. Less air volume will also help to reach the pressure equilibrium faster and hence the sensor's response time will be more efficient. However, due to the small side hole diameter $(20 - 40 \ \mu m)$ and potentially long fiber, surface friction or air viscosity may slow down the flow. It will be a prospective research to analyze these effects with different hole diameters and

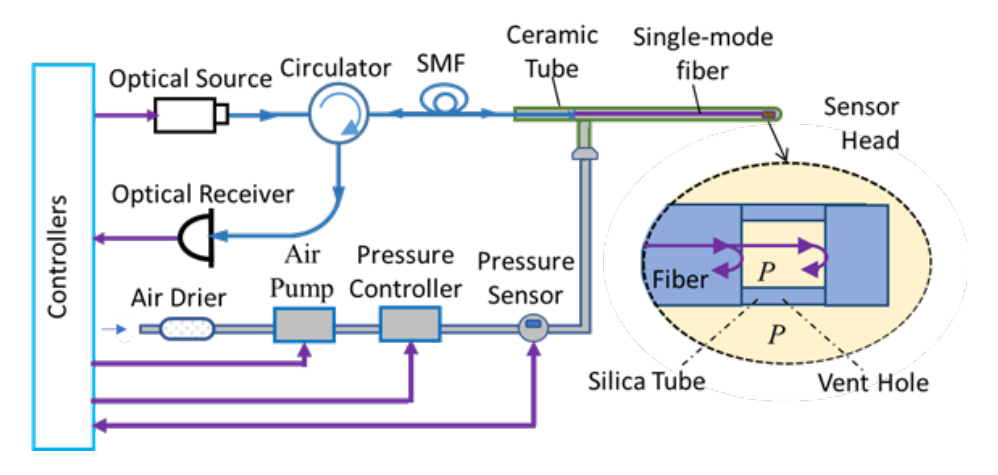


Figure 5.2 Modified setup with an additional air drier to maintain constant humidity.

fiber lengths in order to get faster pressurization time.

2. Analyzing the effect of humidity:

Our method used air as the sensing element, which has provided many advantages we discussed earlier. but in practical application, atmospheric air can contain water vapor, which has a variable refractive index. So, the behavior of water vapor may not be ideal at lower temperatures and/or higher pressure. Water vapor density varies over a relatively large range as the humidity of air can be 20%-100%. A prospective research can focus on determining the effects of changes in air humidity on temperature measurement. To conduct this research, air from an environmental chamber with controlled humidity can be pumped into the sensor cavity. If necessary, an air drier can be applied to the setup to maintain constant humidity (as shown in Figure 5.2) and test its effectiveness.

3. Characterization of accuracy and resolution of the sensor at high temperature:

In our research, we used a thermal tube furnace to test the sensor at high temperatures. This furnace has limitations in temperature tolerance and uniform distribution of heat over the tube. Especially at high temperatures (over 800 °C), this tolerance is deteriorated, which does not provide accurate reflection of our sensor characterization at high temperatures. In future, different methods can be applied to check the sensor's accuracy and resolution for elevated temperature. For example, generating a constant known temperature using melting-point temperature reference is a possible way. Materials with high melting points (mentioned in Table 5.1) can be used for reference.

Table 5.1 High melting point materials for reference

Metal	Melting Point	
Aluminum	660	
Silver	961	
Copper	1083	

5.2 Temperature and strain measurement using cascaded FBG-silicon FPI sensor

5.2.1 Summary

In the second part of our research, we presented a novel FBG-silicon FPI sensor to measure temperature and strain simultaneously. The silicon tip sensor is free from strain and highly sensitive to temperature change (89 pm/°C), thanks to its higher thermal expansion and thermo-optic coefficient than silica. Using this high sensitivity, temperature is first measured. On the other hand, the FBG shift is used to determine the contribution of strain induced by thermal expansion of host structure and applied mechanical strain. We experimentally obtained the thermal strain sensitivity of the FBG as 32 pm/°C and the mechanical strain sensitivity as 1.09 pm/ $\mu\epsilon$, when it is attached to an aluminum beam. The results show high resolution and good linearity up to 100 °C and 150 $\mu\epsilon$.

5.2.2 Future Works

The prospective future research of this work are discussed below:

- 1. Enhancing temperature range: In our current fabrication process, the silicon pillar is attached to the end of the fiber by a glass powder glue, which is cured by UV light. The glass powder used in our work has a low melting point of around 200 °C. Hence we can not characterize our sensor at high temperatures. With the use of a high melting point glass powder or chemical solution as the adhesive for silicon pillar to fiber can increase the temperature range of our sensor. Further research can be conducted to change this fabrication process and characterize the sensor at elevated temperatures.
- **2. Improving thermally induced strain transfer from host to FBG:** In our work, we obtained the thermal strain sensitivity of the FBG as 32 pm/°C when it is attached to an aluminum beam. But

in theory, the thermal expansion of aluminum should provide 45 pm/°C. The expansion-induced strain is not fully transferred to the FBG due to many factors such as the adhesive's length, thickness, Young's modulus, etc. Further research should be carried out to improve the thermal strain transfer from the host to the fiber.

3. Use of sapphire fiber: The use of sapphire fiber instead of silica fiber can make this sensor withstand significantly higher temperatures and provide superior mechanical strength. Further research can be explored in this regard.

BIBLIOGRAPHY

- [1] N. Sabri, S. A. Aljunid, M. S. Salim, and S. Fouad, *Fiber Optic Sensors: Short Review and Applications*, pp. 299–311. Singapore: Springer Singapore, 2015.
- [2] S. Ma, Y. Xu, Y. Pang, X. Zhao, Y. Li, Z. Qin, Z. Liu, P. Lu, and X. Bao, "Optical fiber sensors for high-temperature monitoring: A review," *Sensors*, vol. 22, no. 15, 2022.
- [3] M. Ramakrishnan, G. Rajan, Y. Semenova, and G. Farrell, "Overview of fiber optic sensor technologies for strain/temperature sensing applications in composite materials," *Sensors*, vol. 16, no. 1, 2016.
- [4] S. W. Harun, H. Ahmad, H. Yang, and M. Yasin, *Fiber optic displacement sensors and their applications*. INTECH Open Access Publisher, 2012.
- [5] M. R. Islam, M. M. Ali, M.-H. Lai, K.-S. Lim, and H. Ahmad, "Chronology of fabry-perot interferometer fiber-optic sensors and their applications: A review," *Sensors*, vol. 14, no. 4, pp. 7451–7488, 2014.
- [6] F. Tang, G. Zhou, H.-N. Li, and E. Verstrynge, "A review on fiber optic sensors for rebar corrosion monitoring in rc structures," *Construction and Building Materials*, vol. 313, p. 125578, 2021.
- [7] J. Chen, B. Liu, and H. Zhang, "Review of fiber bragg grating sensor technology," *Frontiers of Optoelectronics in China*, vol. 4, pp. 204–212, 2011.
- [8] T. Yang, C. Liu, X. Liu, Y. Feng, T. Shen, and W. Han, "Fiber optic high temperature sensor based on zno composite graphene temperature sensitive material," *Optics Communications*, vol. 515, p. 128222, 2022.
- [9] Y. Lu and M. Han, "Fiber-optic temperature sensor using dual fabry-perot cavities filled with gas of different pressure," *Sensors and Actuators A: Physical*, vol. 261, pp. 229–234, 2017.
- [10] N. Dong and B. Yang, "Simultaneous measurement of pressure and temperature based on graphene," in *IOP Conference Series: Materials Science and Engineering*, vol. 382, p. 052011, IOP Publishing, 2018.
- [11] Y. Chen and H. Ming, "Review of surface plasmon resonance and localized surface plasmon resonance sensor," *Photonic Sensors*, vol. 2, pp. 37–49, 2012.
- [12] Y. Weng, E. Ip, Z. Pan, and T. Wang, "Single-end simultaneous temperature and strain sensing techniques based on brillouin optical time domain reflectometry in few-mode fibers," *Opt. Express*, vol. 23, pp. 9024–9039, Apr 2015.
- [13] M. Alahbabi, Y. T. Cho, and T. P. Newson, "Comparison of the methods for discriminating temperature and strain in spontaneous brillouin-based distributed sensors," *Opt. Lett.*, vol. 29, pp. 26–28, Jan 2004.
- [14] M. Ghimire and C. Wang, "Highly sensitive fiber loop ringdown strain sensor with low temperature sensitivity," *Measurement Science and Technology*, vol. 28, p. 105101, Sep 2017.

- [15] R. Li, C. Tian, Y. Zhang, J. Zhang, X. Chen, and S. Liu, "Simultaneous measurement of force and temperature by a multi-position fiber loop ringdown sensor array," *Journal of Lightwave Technology*, vol. 33, no. 17, pp. 3607–3612, 2015.
- [16] W.-G. Xie, Y.-N. Zhang, P.-Z. Wang, and J.-Z. Wang, "Optical fiber sensors based on fiber ring laser demodulation technology," *Sensors*, vol. 18, no. 2, p. 505, 2018.
- [17] W. Wang, "Fabry-perot interference fiber acoustic wave sensor based on laser welding all-silica glass," *Materials*, vol. 15, no. 7, 2022.
- [18] Y. P. Georgelin and P. Amram, "A Review of Fabry and Perot Discoveries," in *IAU Colloq. 149: Tridimensional Optical Spectroscopic Methods in Astrophysics* (G. Comte and M. Marcelin, eds.), vol. 71 of *Astronomical Society of the Pacific Conference Series*, p. 382, Jan. 1995.
- [19] D. S. Goodman, *GENERAL PRINCIPLES OF GEOMETRICAL OPTICS*. New York, USA: The McGraw-Hill Companies, Inc., 2010.
- [20] E. V. S. E. K. V. G. D. A. S. V. E. R. N. K. M. V. L. A. G. Tumanovskii, A. L. Shvarts, "Review of the coal-fired, over-supercritical and ultra-supercritical steam power plants," *Thermal Engineering*, vol. 64, pp. 83–96, 2017.
- [21] S. Akdag and H. Yıldırım, "Toward a sustainable mitigation approach of energy efficiency to greenhouse gas emissions in the european countries," *Heliyon*, vol. 6, no. 3, p. e03396, 2020.
- [22] M. Piwowarski, "Optimization of steam cycles with respect to supercritical parameters," *Polish Maritime Research*, vol. 16, no. Special issue, pp. 45–51, 2009.
- [23] "Thermocouples part 1: Emf specifications and tolerances," standard, International Electrotechnical Commission, 2013.
- [24] E. Webster, "A critical review of the common thermocouple reference functions," *Metrologia*, vol. 58, p. 025004, feb 2021.
- [25] D. E. F. L. A. R. C. Janice M. Dulieu-Barton, Leonidas Dokos and M. Sahin, "Deformation and strain measurement techniques for the inspection of damage in works of art," *Studies in Conservation*, vol. 50, no. sup1, pp. 63–73, 2005.
- [26] S. Spolitis, I. Lyashuk, and V. Bobrovs, "Design and performance evaluation of fbg-based temperature sensors network," in 2017 Progress in Electromagnetics Research Symposium Fall (PIERS FALL), pp. 2673–2678, 2017.
- [27] C. V. N. Bhaskar, S. Pal, and P. K. Pattnaik, "Recent advancements in fiber bragg gratings based temperature and strain measurement," *Results in Optics*, vol. 5, p. 100130, 2021.
- [28] Z. Chen, S. Xiong, S. Gao, H. Zhang, L. Wan, X. Huang, B. Huang, Y. Feng, W. Liu, and Z. Li, "High-temperature sensor based on fabry-perot interferometer in microfiber tip," *Sensors*, vol. 18, no. 1, p. 202, 2018.

- [29] Q. Rong, H. Sun, X. Qiao, J. Zhang, M. Hu, and Z. Feng, "A miniature fiber-optic temperature sensor based on a fabry–perot interferometer," *Journal of optics*, vol. 14, no. 4, p. 045002, 2012.
- [30] L. Li, Z. Feng, X. Qiao, H. Yang, R. Wang, D. Su, Y. Wang, W. Bao, J. Li, Z. Shao, *et al.*, "Ultrahigh sensitive temperature sensor based on fabry–pérot interference assisted by a graphene diaphragm," *IEEE Sensors Journal*, vol. 15, no. 1, pp. 505–509, 2014.
- [31] T. Liu, J. Yin, J. Jiang, K. Liu, S. Wang, and S. Zou, "Differential-pressure-based fiber-optic temperature sensor using fabry–perot interferometry," *Optics letters*, vol. 40, no. 6, pp. 1049–1052, 2015.
- [32] W. Wang, X. Zhou, W. Wu, J. Chen, S. He, W. Guo, J. Gao, S. Huang, and X. Chen, "Monolithic structure-optical fiber sensor with temperature compensation for pressure measurement," *Materials*, vol. 12, no. 4, p. 552, 2019.
- [33] M. S. Ferreira, L. Coelho, K. Schuster, J. Kobelke, J. L. Santos, and O. Frazão, "Fabry–perot cavity based on a diaphragm-free hollow-core silica tube," *Optics letters*, vol. 36, no. 20, pp. 4029–4031, 2011.
- [34] M. Szczerska, "Temperature sensors based on polymer fiber optic interferometer," *Chemosensors*, vol. 10, no. 6, p. 228, 2022.
- [35] D. Jáuregui-Vázquez, J. M. Estudillo-Ayala, R. Rojas-Laguna, E. Vargas-Rodríguez, J. M. Sierra-Hernández, J. C. Hernández-García, and R. I. Mata-Chávez, "An all fiber intrinsic fabry-perot interferometer based on an air-microcavity," *Sensors*, vol. 13, no. 5, pp. 6355–6364, 2013.
- [36] R. Flores, R. Janeiro, and J. Viegas, "Optical fibre fabry-pérot interferometer based on inline microcavities for salinity and temperature sensing," *Scientific reports*, vol. 9, no. 1, p. 9556, 2019.
- [37] J. Wang, B. Dong, E. Lally, J. Gong, M. Han, and A. Wang, "Multiplexed high temperature sensing with sapphire fiber air gap-based extrinsic fabry–perot interferometers," *Optics letters*, vol. 35, no. 5, pp. 619–621, 2010.
- [38] Y. Chen, Y. Zheng, H. Xiao, D. Liang, Y. Zhang, Y. Yu, C. Du, and S. Ruan, "Optical fiber probe microcantilever sensor based on fabry–perot interferometer," *Sensors*, vol. 22, no. 15, p. 5748, 2022.
- [39] F. Tang, Z. Li, Y. Tang, Y. Chen, and H.-N. Li, "Simultaneous measurement of shrinkage and coefficient of thermal expansion of mortar based on efpi sensors with nanometer resolution," *Measurement*, vol. 152, p. 107376, 2020.
- [40] A. Hokkanen, A. Salmi, V. Vashistha, M. Nyman, S. K. Nielsen, T. Jensen, M. Jessen, B. Wälchli, M. Kapulainen, V. Naulin, *et al.*, "A panda fiber temperature sensor up to 900° c," *Journal of Instrumentation*, vol. 17, no. 07, p. P07031, 2022.

- [41] J. E. Antonio-Lopez, Z. S. Eznaveh, P. LiKamWa, A. Schülzgen, and R. Amezcua-Correa, "Multicore fiber sensor for high-temperature applications up to 1000 c," *Optics letters*, vol. 39, no. 15, pp. 4309–4312, 2014.
- [42] S. Korposh, S. W. James, S.-W. Lee, and R. P. Tatam, "Tapered optical fibre sensors: Current trends and future perspectives," *Sensors*, vol. 19, no. 10, p. 2294, 2019.
- [43] X. Zhang, Y. Xu, X.-S. Zhu, and Y.-W. Shi, "Surface plasmon resonance temperature sensor with tunable detection range based on a silver-coated multi-hole optical fiber," *Opt. Express*, vol. 30, pp. 48091–48102, Dec 2022.
- [44] S. Weng, L. Pei, J. Wang, T. Ning, and J. Li, "High sensitivity d-shaped hole fiber temperature sensor based on surface plasmon resonance with liquid filling," *Photonic Research*, vol. 5, pp. 103–107, Apr 2017.
- [45] Y. Chen and H. Ming, "Review of surface plasmon resonance and localized surface plasmon resonance sensor," *Photonic Sensors*, vol. 2, pp. 37–49, 2012.
- [46] R. Eisermann, S. Krenek, G. Winzer, and S. Rudtsch, "Photonic contact thermometry using silicon ring resonators and tuneable laser-based spectroscopy," *tm Technisches Messen*, vol. 88, no. 10, pp. 640–654, 2021.
- [47] S. Zhang, Y. Mei, T. Xia, Z. Cao, Z. Liu, and Z. Li, "Simultaneous measurement of temperature and pressure based on fabry-perot interferometry for marine monitoring," *Sensors*, vol. 22, no. 13, p. 4979, 2022.
- [48] D. Polyzos, J. Mathew, W. N. MacPherson, and R. R. J. Maier, "Effect of dopant diffusion on the long-term stability of fabry–pérot optical fiber sensors," *Journal of Lightwave Technology*, vol. 35, no. 24, pp. 5317–5323, 2017.
- [49] A. Yablon, M. Yan, P. Wisk, F. DiMarcello, J. Fleming, W. Reed, E. Monberg, D. DiGiovanni, J. Jasapara, and M. Lines, "Refractive index perturbations in optical fibers resulting from frozen-in viscoelasticity," *Applied physics letters*, vol. 84, no. 1, pp. 19–21, 2004.
- [50] A. A. Yakusheva, "Devitrification kinetics and optical stability of optical fibers at high temperatures," masters thesis, Virginia Tech, June 2018.
- [51] D. Grobnic, C. Hnatovsky, S. Dedyulin, R. B. Walker, H. Ding, and S. J. Mihailov, "Fiber bragg grating wavelength drift in long-term high temperature annealing," *Sensors*, vol. 21, no. 4, 2021.
- [52] Y. Cui, Y. Jiang, T. Liu, J. Hu, and L. Jiang, "A dual-cavity fabry–perot interferometric fiber-optic sensor for the simultaneous measurement of high-temperature and high-gas-pressure," *IEEE Access*, vol. 8, pp. 80582–80587, 2020.
- [53] P. Xia, Y. Tan, C. Yang, Z. Zhou, and K. Yun, "A composite fabry-perot interferometric sensor with the dual-cavity structure for simultaneous measurement of high temperature and strain," *Sensors*, vol. 21, no. 15, p. 4989, 2021.

- [54] S. Pevec and D. Donlagic, "Miniature all-fiber fabry–perot sensor for simultaneous measurement of pressure and temperature," *Applied optics*, vol. 51, no. 19, pp. 4536–4541, 2012.
- [55] Y. Jiang, "Fourier transform white-light interferometry for the measurement of fiber-optic extrinsic fabry–perot interferometric sensors," *IEEE Photonics Technology Letters*, vol. 20, no. 2, pp. 75–77, 2007.
- [56] B. Zhang, X. Tong, P. Hu, Q. Guo, Z. Zheng, and C. Zhou, "Wavelet phase extracting demodulation algorithm based on scale factor for optical fiber fabry-perot sensing," *Optics Express*, vol. 24, no. 26, pp. 29506–29511, 2016.
- [57] J. Cui, Y. Niu, H. Dang, K. Feng, X. Sun, and J. Tan, "Demodulation method of fp sensor based on wavelet transform and polarization low coherence interferometry," *Sensors*, vol. 20, no. 15, p. 4249, 2020.
- [58] P. Zhang, Y. Wang, Y. Chen, X. Lei, Y. Qi, J. Feng, and X. Liu, "A high-speed demodulation technology of fiber optic extrinsic fabry-perot interferometric sensor based on coarse spectrum," *Sensors*, vol. 21, no. 19, p. 6609, 2021.
- [59] Y. Lu, M. Han, and J. Tian, "Fiber-optic temperature sensor using a fabry–pérot cavity filled with gas of variable pressure," *IEEE Photonics Technology Letters*, vol. 26, no. 8, pp. 757–760, 2014.
- [60] H. R. Chowdhury and M. Han, "Fiber optic temperature sensor system using air-filled fabry–pérot cavity with variable pressure," *Sensors*, vol. 23, no. 6, 2023.
- [61] P. E. Ciddor, "Refractive index of air: new equations for the visible and near infrared," *Applied optics*, vol. 35, no. 9, pp. 1566–1573, 1996.
- [62] G. Liu, M. Han, and W. Hou, "High-resolution and fast-response fiber-optic temperature sensor using silicon fabry-pérot cavity," *Optics express*, vol. 23, no. 6, pp. 7237–7247, 2015.
- [63] H. R. Chowdhury and M. Han, "Fiber optic temperature sensor using dual air-filled fabry-pérot cavities with variable pressure," *IEEE Photonics Technology Letters*, vol. 35, no. 24, pp. 1327–1330, 2023.
- [64] H. Rocha, C. Semprimoschnig, and J. P. Nunes, "Sensors for process and structural health monitoring of aerospace composites: A review," *Engineering Structures*, vol. 237, p. 112231, 2021.
- [65] T. Liu, L. Liu, G.-y. Gou, Z. Fang, J. Sun, J. Chen, J. Cheng, M. Han, T. Ma, C. Liu, and N. Xue, "Recent advancements in physiological, biochemical, and multimodal sensors based on flexible substrates: Strategies, technologies, and integrations," *ACS Applied Materials & Interfaces*, vol. 15, no. 18, pp. 21721–21745, 2023. PMID: 37098855.
- [66] C. G. Watson, J., "A review of high-temperature electronics technology and applications," *Journal of Materials Science: Materials in Electronics*, vol. 26, p. 9226–9235, 2015.
- [67] S.-C. Her and W.-N. Lin, "Simultaneous measurement of temperature and mechanical strain using a fiber bragg grating sensor," *Sensors*, vol. 20, no. 15, 2020.

- [68] K. Guo, J. He, L. Shao, G. Xu, and Y. Wang, "Simultaneous measurement of strain and temperature by a sawtooth stressor-assisted highly birefringent fiber bragg grating," *Journal of Lightwave Technology*, vol. 38, no. 7, pp. 2060–2066, 2020.
- [69] Q. Tian, G. Xin, K.-S. Lim, Y.-J. Ee, F. Xue, Y. He, J. Zhu, H. Ahmad, X. Liu, and H. Yang, "Optical fiber sensor with double tubes for accurate strain and temperature measurement under high temperature up to 1000 °c," *IEEE Sensors Journal*, vol. 22, no. 12, pp. 11710–11716, 2022.
- [70] J. Tian, Y. Jiao, S. Ji, X. Dong, and Y. Yao, "Cascaded-cavity fabry–perot interferometer for simultaneous measurement of temperature and strain with cross-sensitivity compensation," *Optics Communications*, vol. 412, pp. 121–126, 2018.
- [71] X. Fu, L. Liu, S. Ma, G. Fu, W. Jin, and W. Bi, "Dual-parameter four-beam interferometric sensor for the measurement of temperature and strain with a double air-gaps structure based on graded-index few mode fiber," *OSA Continuum*, vol. 2, pp. 3381–3392, Dec 2019.
- [72] W. Jin, W. C. Michie, G. Thursby, M. Konstantaki, and B. Culshaw, "Simultaneous measurement of strain and temperature: error analysis," *Optical Engineering*, vol. 36, no. 2, pp. 598 609, 1997.
- [73] A. D. Gomes, M. S. Ferreira, J. Bierlich, J. Kobelke, M. Rothhardt, H. Bartelt, and O. Frazão, "Optical harmonic vernier effect: A new tool for high performance interferometric fiber sensors," *Sensors*, vol. 19, no. 24, 2019.
- [74] T. P. ao, F. Araújo, and P. Antunes, "Highly sensitive fiber optic temperature and strain sensor based on an intrinsic fabry–perot interferometer fabricated by a femtosecond laser," *Opt. Lett.*, vol. 44, pp. 4833–4836, Oct 2019.
- [75] L. Hou, C. Zhao, B. Xu, B. Mao, C. Shen, and D. N. Wang, "Highly sensitive pdms-filled fabry–perot interferometer temperature sensor based on the vernier effect," *Appl. Opt.*, vol. 58, pp. 4858–4865, Jun 2019.
- [76] J. M. Gere and S. P. Timoshenko, *Mechanics of Materials*. Belmont, California: Wadsworth, Inc., 1984.
- [77] M. Liang, N. Chen, X. Fang, and G. Wu, "Strain transferring mechanism analysis of the surface-bonded fbg sensor," vol. 57, pp. 5837–5843, July 2018.